The Rapidly Flaring Afterglow of the Very Bright and Energetic GRB 070125

Adria C. Updike[1], Josh B. Haislip[2], Melissa C. Nysewander[3], Andrew S. Fruchter[3], D. Alexander Kann[4], Sylvio Klose[4], Peter A. Milne[5], G. Grant Williams[6], Weikang Zheng[7], Carl W. Hergenrother[8], Jason X. Prochaska[9], Jules P. Halpern[10], Nestor Mirabal[10], John R. Thorstensen[11], Alexander J. van der Horst[12], Rhaana L. C. Starling[13], Judith L. Racusin[14], David N. Burrows[14], N. P. M. Kuin[15], Peter W. A. Roming[14], Eric Bellm[16], Kevin Hurley[16], Weidong Li[17], Alexei V. Filippenko[17], Cullen Blake[18], Dan Starr[17], Emilio E. Falco[19], Warren R. Brown[18], Xinyu Dai[20], Jinsong Deng[7], Liping Xin[7], Yulei Qiu[7], Jianyan Wei[7], Yuji Urata[21,22], Domenico Nanni[23,24], Elisabetta Maiorano[25], Eliana Palazzi[25], Giuseppe Greco[26], Corrado Bartolini[26], Adriano Guarnieri[26], Adalberto Piccioni[26], Graziella Pizzichini[25], Federica Terra[23], Kuntal Misra[27,28], B. C. Bhatt[29], G. C. Anupama[30] X. Fan[5], L. Jiang[5], Ralph A. M. J. Wijers[31], Daniel E. Reichart[2], Hala A. Eid[1], Ginger Bryngelson[1], Jason Puls[1], R. C. Goldthwaite[1], and Dieter H. Hartmann[1]

[1]Department of Physics and Astronomy, Clemson University 118 Kinard Laboratory, Clemson, SC 29634.

[2]Department of Physics and Astronomy, University of North Carolina at Chapel Hill, Campus Box 3255, Chapel Hill, NC 27599.

[3]Space Telescope Science Institute, 3700 San Martin Dr., Baltimore, MD 21218.

[4]Thüringer Landessternwarte Tautenburg, Sternwarte 5, D–07778 Tautenburg, Germany.

[5]Steward Observatory, University of Arizona, Tucson AZ 85721-0065.

[6]MMT Observatory, University of Arizona, Tucson AZ 85721-0065.

[7]National Astronomical Observatories, 20A Datun Rd., Chaoyang Dist., Beijing 100012, China.

[8]Lunar and Planetary Laboratory, University of Arizona, Tucson AZ 85721-0092.

[9]UCO/Lick Observatory, University of California, Santa Cruz, CA 95064.

[10]Columbia Astrophysics Laboratory, Columbia University, 550 West 120th Street, New York, NY 10027.

[11]Dept. of Physics and Astronomy, Dartmouth College 6127 Wilder Laboratory Hanover, NH 03755-3528.

[12]NASA Postdoctoral Program Fellow, NSSTC, 320 Sparkman Drive, Huntsville, AL 35805.

[13]Department of Physics and Astronomy, University of Leicester, University Road, Leicester, LE1 7RH, UK.

[14]Penn State University, Department of Astronomy & Astrophysics, 525 Davey Lab, University Park, PA 16802.

[15]Mullard Space Science Laboratory/UCL, Holmbury St. Mary, Dorking, Surrey, HR5, 6NT, UK.

[16]University of California, Space Sciences Laboratory, 7 Gauss Way, Berkeley, CA 94720-7450.

[17]Department of Astronomy, University of California, Berkeley, CA 94720-3411.

[18]Harvard-Smithsonian Center for Astrophysics, 60 Garden Street, MS-20, Cambridge, MA 02138.

[19]Smithsonian Institution, Whipple Observatory, 670 Mt. Hopkins Road, P.O. Box 6369, Amado, AZ 85645.

[20]Ohio State University Department of Physics, 191 W. Woodruff Ave, Columbus, OH 43210-1117.

[21]Dept. of Physics, Saitama University, Shimookubo, Urawa 338-8570 Japan.

[22]Academia Sinica Institute of Astronomy and Astrophysics, Taipei 106, Taiwan, Republic of China.

[23]Second University of Roma "Tor Vergata," Italy.

[24]INAF/OAR.

[25]INAF/IASF Bologna, via Gobetti 101, 40129 Bologna, Italy.

[26]Dipartimento di Astronomia, Universite di Bologna, via Ranzani 1, 40127 Bologna, Italy.

[27]Aryabhatta Research Institute of observational sciencES (ARIES), Manora Peak, Nainital - 263 129

ABSTRACT

We report on multi-wavelength observations, ranging from X-ray to radio wave bands, of the IPN-localized gamma-ray burst GRB 070125. Spectroscopic observations reveal the presence of absorption lines due to O I, Si II, and C IV, implying a likely redshift of $z = 1.547$. The well-sampled light curves, in particular from 0.5 to 4 days after the burst, suggest a jet break at 3.7 days, corresponding to a jet opening angle of $\sim$7.0°, and implying an intrinsic GRB energy in the 1–10,000 keV band of around $E_\gamma = (6.3 - 6.9) \times 10^{51}$ erg (based on the fluences measured by the gamma-ray detectors of the IPN network). GRB 070125 is among the brightest afterglows observed to date. The spectral energy distribution implies a host extinction of $A_V < 0.9$ mag. Two rebrightening episodes are observed, one with excellent time coverage, showing an increase in flux of 56% in $\sim$8000 seconds. The evolution of the afterglow light curve is achromatic at all times. Late-time observations of the afterglow do not show evidence for emission from an underlying host galaxy or supernova. Any host galaxy would be subluminous, consistent with current GRB host-galaxy samples. Evidence for strong Mg II absorption features is not found, which is perhaps surprising in view of the relatively high redshift of this burst and the high likelihood for such features along GRB-selected lines of sight.

Subject headings: gamma-ray bursts: GRB 070125

1. Introduction

Since the detection of the first gamma-ray burst (GRB) in 1967 with detectors aboard the Vela satellites (Klebesadel et al. 1973), our understanding of the nature of this still somewhat mysterious phenomenon went through several major advances. In particular, the establishment of their cosmological distances via ground-based follow-up spectroscopy of

---

India.

[28]Inter University Center for Astronomy and Astrophysics, Post Bag 4, Ganeshkhind, Pune 411 007 India.

[29]Center for Research and Education in Science and Technology (CREST), Hosakote, Bangalore - 562 114 India.

[30]Indian Institute of Astrophysics, Bangalore - 560 034 India.

[31]Astronomical Institute, University of Amsterdam, Kruislaan 403, 1098 SJ Amsterdam, The Netherlands.

their afterglow emission, first accomplished for GRB 970508 (Metzger et al. 1997) at a redshift of $z = 0.835$, led to a spectacular world-wide effort to accumulate prompt and afterglow observations which have yielded many surprises and breakthrough discoveries. One decade after the first afterglow was discovered with BeppoSAX (Costa et al. 1997; van Paradijs et al. 1997), the accumulated sample of about 500 GRBs[1] exhibits X-ray, optical, and radio afterglows to varying degrees. Their observed redshift distribution (Jakobsson et al. 2006) is very broad, with more than half of the GRBs at distances beyond the peak of the cosmic star formation rate at $z \sim 1 - 2$, and with GRB 050904 at $z = 6.29$ currently being the most distant burst (Haislip et al. 2006; Kawai et al. 2006). The association of long-duration GRBs with Type Ib/c supernovae (see Filippenko 1997 for a review of supernova classification), established in a few cases via direct spectroscopy and in a larger sample via a late extra emission component revealed in broad-band photometric observations (e.g., Galama et al. 1998; Hjorth et al. 2003; Stanek et al. 2003b; Zeh et al. 2004; Malesani et al. 2004; Pian et al. 2006; Mirabal et al. 2006; Woosley & Bloom 2006) has thus opened promising observational windows into star formation in the universe (e.g., Bromm & Loeb 2006), cosmic chemical evolution via absorption-line spectroscopy of intervening clouds and host galaxies (e.g., Savaglio 2006; Berger et al. 2006), and may eventually provide valuable constraints on the cosmic re-ionization history in the crucial $z > 6$ epoch (e.g., Fan et al. 2006; Totani et al. 2006; Gallerani et al. 2007; McQuinn et al. 2007). Every new GRB provides yet another opportunity to investigate these topics, or the GRB environment via features in the afterglow power-law decay, or to add key data to enable a better understanding of their statistical properties and morphological classification.

Here we report on follow-up observations of GRB 070125, which was discovered by detectors aboard the IPN members Mars Odyssey, Suzaku, INTEGRAL, Konus-Wind, and RHESSI at T_0 = 07:20:42 (UT dates and times are used throughout this paper) on January 25, 2007 (Hurley et al. 2007). The BAT detector aboard *Swift* (Gehrels et al. 2004) recorded the burst during a slew, and therefore did not trigger. The BAT position is consistent with the IPN localization. The position was monitored with the XRT from 0.54 to 18.5 days after T_0. We report these observations and their implications (see also Racusin et al. 2007a), as well as the results obtained from ground-based follow-up observations with a large group of small, mid-sized, and large-aperture telescopes. As observed by RHESSI, GRB 070125 had a duration of T_{90}=63.0 $\pm$ 1.7 seconds (Bellm et al. 2007b), and thus clearly belongs in the class of long-(soft) GRBs (e.g., Kouveliotou et al. 1993). Details of the prompt emission can be found in Bellm et al. (2007b). From a joint fit to the RHESSI and Konus data, Bellm et al. (2007b) derived isotropic energies in the 1 keV $-$ 10 MeV band of $(9.44^{+0.40}_{-0.41}) \times 10^{53}$ erg

[1]See the compilation in http://www.mpe.mpg.de/~jcg/grbgen.html

(Konus) and $(8.27 \pm 0.39) \times 10^{53}$ erg (RHESSI).

Starting with our early response using the 0.9 m SARA telescope and the 2.3 m Bok telescope on Kitt Peak, we compile observations from a large set of follow-up programs to establish the afterglow light-curve properties. We analyze a diverse set of data with a uniform analysis method to reduce any scatter and establish a well-sampled light curve (which is usually not possible with data from a single telescope). We obtained Keck-I spectra to establish a burst redshift of $z = 1.547$ (which agrees with the value derived from Gemini-North spectroscopy, Cenko et al. 2007a). The afterglow initially appeared to have a jet break around day 1.5, but the analysis presented here shows that at this time multiple rebrightening episodes occur, which are in fact better fit with abrupt jumps in the flux, and not the usual jet-break. However, the available sparse late-time data do indicate that a break in fact does take place, at ~ 3.7 days after the burst, which agrees with the radio light curve at 4.8 GHz presented here, spanning a time range from 1.5 to 278 days after the burst.

We discuss how these observations place GRB 070125 into the context of other gamma-ray bursts and how the late-time observations may constrain the properties of the underlying host and a potential supernova that is expected to reach its light maximum $\sim 10(1+z)$ days after gamma-ray emergence. Emission was detected from this source with the LBT at $t = 26.8$ days (Garnavich et al. 2007; Dai et al. 2007), but the flux is too large to be explained with emission from the commonly assumed SN 1998bw-like template at the burst redshift of 1.547, and we instead consider the LBT detection to be the afterglow. This interpretation is supported by a second-epoch LBT observation ($R > 26.1$ mag) which did not result in a detection (Dai et al. 2007).

The paper is organized as follows. In §2 we describe our set of observations of GRB 070125, from early X-ray and UVOT data from *Swift* to late-time optical observations with the 8.4m LBT and late-time radio observations with the WSRT. In §3, we describe the data analysis and results derived from the multi-wavelength data, and in §4 we discuss the implications of this combined data set. In particular, we discuss GRB 070125 in the context of the existing data on afterglow emission properties, and we examine the implied burst energies in light of the standard models for long-soft GRBs and their interactions with the circumburst medium.

2. Observations

GRB 070125 was detected at 07:20:42 on January 25, 2007, by Mars Odyssey (HEND and GRS), Suzaku (WAM) (Yamaoka et al. 2005, Yamaoka 2008 in prep.), INTEGRAL (SPI-ACS), KONUS, and RHESSI (Hurley et al. 2007). The *Swift* satellite detected the

burst, but did not trigger because *Swift* was slewing. The GRB entered the coded field of view of the *Swift* BAT 6 minutes after the trigger time, and ground processing revealed a significant source at the intersection of the IPN annuli, strongly reducing the error box. The Burst Alert Telescope (BAT) (Barthelmy et al. 2005) produced a refined J2000 location of $\alpha = 7^{\rm h}\ 51^{\rm m}\ 24^{\rm s}$, $\delta = +31^\circ\ 08'\ 24''$ based on data taken about 6 minutes after T_0 (Racusin et al. 2007c). About 13 hours later, *Swift* began observing GRB 070125 as a target of opportunity observation. The afterglow was discovered with the Palomar 1.5 m telescope (Cenko & Fox 2007) and produced an accurate afterglow location of $\alpha = 7^{\rm h}\ 51^{\rm m}\ 17^{\rm s}$, $\delta = +31^\circ\ 09'\ 04''$ ($\pm$ $0.5''$ in each coordinate).

Below, we describe space-based observations with instruments on the *Swift* satellite, as well as ground-based photometric and spectroscopic observations. Figure 1 shows a false-color image of the field derived from BVR observations with the Bok telescope (described in greater detail below). The afterglow shown in the image within the circle has a brightness of $R = 18.7$ mag at one day after the burst. The field has a relatively low star density (Galactic coordinates $l = 189.4^\circ$, $b = 25.6^\circ$) and has only a little foreground extinction of $E(B-V) = 0.052$ mag, $A_V = 0.16$ mag (Schlegel et al. 1998).

2.1. Space-Based Observations

The space-based observations reported in this section consist of ultraviolet, optical, and X-ray data, carried out by the UVOT and XRT instruments on $Swift$ beginning 12.97 hours after the burst trigger. The afterglow was detected in the X-ray band and all six UVOT filters, ranging from V to uvw2 (central wavelengths of 546 nm and 193 nm, respectively).

2.1.1. XRT Observations

Although GRB 070125 was detected by the *Swift*-BAT in ground analysis, the BAT did not trigger due to the occurrence of the burst during a pre-planned slew phase, and consequently the narrow-field instruments did not obtain prompt observations. *Swift* began Target of Opportunity observations of GRB 070125 about 13 hours after the trigger at 20:18:48 January 25, 2007.

The X-ray afterglow was initially detected by the XRT (Burrows et al. 2005) in the first few orbits of observation and was followed up for 18.5 days post-trigger until the afterglow was no longer detected by the XRT. The total exposure time of GRB 070125 with the XRT was 170 ks. All observations used the Photon Counting (PC) mode due to the low count rate

of the source. Level-1 data products were downloaded from the NASA/GSFC *Swift* Data Center (SDC) and processed using XRTDAS software (v2.0.1). The *xrtpipeline* task was used to generate level-2 cleaned event files. Only events with PC grades 0–12 and energies in the range $0.3 - 10.0$ keV were used in subsequent temporal and spectral analysis.

The XRT light curve was created by extracting the counts in a circular region around the afterglow position with a variable radius designed to optimize the signal-to-noise ratio (S/N) depending on the count rate. A region with 40 pixels radius clear of serendipitous background sources was used to estimate the contribution of background counts in the source extraction region. The number of counts per bin was chosen depending on the count rate to show sufficient detail with reasonable error bars. Background-subtracted count rates were also corrected for the portion of the PSF excluded by the extraction region and any proximity to bad columns and hot pixels in the XRT CCD. Pile-up is negligible at these flux levels.

We carried out spectral analysis on this data set to obtain a counts-to-flux conversion for the purpose of creating an XRT light curve in standard units. Spectral analysis was carried out using XSPEC (v12.3.1) and the XRT ancillary response file created with the standard *xrtmkarf* task using the response matrix file swxpc0to12s0_20010101v010.rmf from CALDB (release 2007-12-04). We fit the spectrum to a simple absorbed power law with an absorption system at $z = 0$ fixed to the Galactic HI column density (4.8×10^{20} cm^{-2}, Dickey & Lockman 1990), and allowed the absorption at the host-galaxy redshift ($z = 1.547$) to vary. The resulting fit to the PC spectrum gave an intrinsic effective hydrogen column density of $N_H = 0.19^{+0.20}_{-0.18} \times 10^{22}$ cm^{-2} and a photon index of $2.00^{+0.15}_{-0.14}$, with a reduced χ^2 of 0.67 (29 degrees of freedom [d.o.f.]). The absorption column is in excess of the Galactic foreground value, suggesting the possibility that the host galaxy or the circumburst medium contribute somewhat to the observed extinction. We address this issue below with the X-ray/optical/near-IR afterglow spectral energy distribution (SED). The mean absorbed (unabsorbed) flux is 3.9×10^{-13} erg cm^{-2} s^{-1} (4.7×10^{-13} erg cm^{-2} s^{-1}) with a corresponding mean count rate of 9.0×10^{-3} counts s^{-1}. The resulting light curve is shown (arbitrarily scaled) in Figure 2.

2.1.2. UVOT Observations

The UVOT (Roming et al. 2005) began observing 13 hours after the trigger. The data were retrieved from the *Swift* archive at GSFC. Data taken in the uvm2 filter had not all been aspect-corrected, but inspection of the individual images showed that the sources fell within their $3''$ radius region files. The counts were measured twice, using XIMAGE and UVOTMAGHIST, the latter during testing of the software updates for HEADAS version 6.3.

The measurements were made for 3″ and 5″ radius apertures, both for the transient as well as for four field stars. Following the recommendations in Poole et al. (2008), an aperture correction was derived based on the observations of field stars having count rates of 1–10 ct/s, sufficiently low that the point-spread function (PSF) is not considered to be affected by the UVOT coincidence loss. The calibration of Poole et al. (2008) was used (CALDB update of 2007-07-11).

Since the UVOT is a photon-counting instrument, subsequent images can be co-added to improve the S/N. This was done by writing software to co-add the counts until a desired value of S/N was found as well as optimizing the time resolution. We checked that there was no noticeable difference in co-adding counts before or after doing background subtraction or coincidence-loss corrections, as expected for the low count rates of the transient. The measurement error of the UVOT is Binomial due to the finite number of frames in an observation, and the errors were calculated accordingly with the formula given by Kuin & Rosen (2008). Magnitudes were derived using the new zeropoints of Poole et al. (2008).

The UVOT images of GRB 070125 were further reduced following the recipe outlined by Li et al. (2006), which provided an independent photometric calibration to the U, B, and V filters employing a small aperture (radius of 2.5″) for photometry (thus no need to do aperture correction). Comparison between the two reductions indicates that the measurements are consistent with each other within the uncertainties.

2.2. Ground-Based Observations

2.2.1. Ground-Based Afterglow Photometry

The GCN burst notice (Hurley et al. 2007) was sent out at 21:46:48 Jan 25, approximately 13 hours and 26 minutes after the burst had been detected by the IPN. The SARA 0.9 m telescope on Kitt Peak began imaging of the field of GRB 070125 in the V band ~ 19 hours and 15 minutes after the trigger time, and was closely followed by the 0.41 m PROMPT telescope on Cerro Tololo (20 hours and 34 minutes) in $BVRI$ and the Bok 2.3 m telescope on Kitt Peak in V (24 hours). An afterglow candidate was detected by Cenko & Fox (2007) in the Palomar 1.5 m images. Further observations were obtained with TNT, EST, SOAR, MDM, MMT, Kuiper, Loiano, KAIT, PAIRITEL, TNG, HCT, and the LBT (see Table 1). Observations around 4 days after the trigger were hampered by the full Moon, which may explain why many telescopes stopped observing at that time.

The SARA (Southeastern Association for Research in Astronomy) 0.9 m telescope is located on Kitt Peak. SARA observations were carried out for three days following the burst

until the afterglow was no longer detectable (Updike et al. 2007). Observations with SARA were limited to the V band using the SARA Apogee Alta U47 camera.

The Bok 2.3 m telescope is located at Kitt Peak National Observatory (KPNO) and is operated by the University of Arizona Steward Observatory. Bok observations utilized the 90prime instrument (Williams et al. 2004) and provide $BVRI$ data. Supplemental observations were obtained by the Kuiper Mont4k Imager on the Kuiper 1.54 m telescope (located on Mt. Bigelow in Arizona) in the R band.

PROMPT observations were carried out in $BVRI$ by one of the five PROMPT (Panchromatic Optical Monitoring and Polarimetry Telescopes) telescopes located on Cerro Tololo, Chile. PROMPT5 is a 0.41 m Ritchey-Chrétien telescope outfitted with a rapid-readout Apogee Alta U47+ camera (Haislip et al. 2007).

The MDM observations were taken with the 2.4 m and 1.3 m Hiltner telescopes on Kitt Peak, a SITe backside-illuminated CCD, and VRI filters.

Observations from the Loiano 1.52 m telescope of the Bologna Astronomical Observatory, located at Loiano (Italy), were taken in the Cousins R band equipped with BFOSC, a multi-purpose instrument for imaging and spectroscopy (Greco et al. 2007).

The 0.8 m TNT telescope and 1 m EST telescope are located at Xinglong Observatory of the National Astronomical Observatories of China. Each telescope is equipped with a Princeton Instruments 1340×1300 pixel CCD. Observations were carried out in the R and V bands. Observational details can be found in Deng & Zheng (2006).

The 3.58 m Telescopio Nazionale Galileo (TNG) is located at La Palma in the Canary Islands (Spain). TNG was equipped with the spectrophotometer DOLoRES (Device Optimized for the LOw RESolution) operating in imaging mode with a scale of $0.275''$ pixel^{-1}.

The KAIT (Katzman Automatic Imaging Telescope; Filippenko et al. 2001) 0.76 m data are unfiltered, and were obtained with an Apogee AP7 camera. Li et al. (2003) demonstrated that the KAIT unfiltered magnitudes can be reliably transformed to the standard Cousins R band with a precision of $\sim$5%, if the color of the object is known. Since we have reliable color information for GRB 070125 during the time of the KAIT observations, we calibrated the KAIT data to the R band following the procedure in Li et al. (2003).

The SOAR (Southern Observatory for Astrophysical Research) 4.1 m telescope is located on Cerro Pachon, Chile. SOAR observations were taken in the near-IR using OSIRIS (Ohio State InfraRed Imager/Spectrometer).

PAIRITEL (Peters Automated Infrared Imaging Telescope) is a 1.3 m telescope located

on Mt. Hopkins in Arizona. It is a robotic telescope which allows for rapid follow-up IR imaging of GRB targets. The PAIRITEL observations were taken in the near-IR using a 2MASS instrument.

The MMT is located at the Whipple Observatory on Mt. Hopkins in Arizona. It is a 6.5 m telescope which contributed near-IR observations, obtained with SWIRC, the SAO Widefield Infrared Camera.

Optical observations of the afterglow were carried out by the 2.01 m Himalayan Chandra Telescope (HCT) at the Indian Astronomical Observatory (IAO), Hanle (India). The CCD used at HCT was a 2048 × 4096 pixel SITe chip mounted on the Himalayan Faint Object Spectrograph Camera (HFOSC). Filters used are Bessell V, R and I.

The images were reduced and stacked where appropriate. Optical calibration was performed using IRAF PSF photometry and comparison to 15 standard stars, whose magnitudes were obtained through a field calibration using Graham standard stars (Graham 1982) and the Hardie method (Hiltner 1964). Near-IR images were reduced in IRAF using standard reduction pipelines. The MMT images were calibrated relative to standards observed during the same night, and the SOAR images were calibrated relative to the Graham standard stars. LBT (Large Binocular Telescope) data cited are derived from Garnavich et al. (2007) and Dai et al. (2007). Note that the Sloan r' observation has been converted to the R band. All observations carried out by this collaboration can be found in Table 1.

2.2.2. Ground-Based Afterglow Spectroscopy

We observed the afterglow of GRB 070125 with the Keck-I LRIS double spectrograph (Oke et al. 1995) through a long slit 1.0″ wide starting at 05:44:05 on January 26. Two 600 s exposures were acquired using the D560 dichroic, the 400/3400 grism, and the 600/5000 grating. This instrumental configuration yields nearly continuous spectra over the range 3000–8000 Å at a spectral resolution (full width at half-maximum intensity; FWHM) of ∼8 Å on the blue side and ∼6 Å on the red side. The data were reduced using standard procedures (bias subtracted, flat-fielded) and extracted with a boxcar encompassing ∼90% of the flux.

2.2.3. Ground-Based Radio Observations

Radio observations were performed with the Westerbork Synthesis Radio Telescope (WSRT) at 1.4, 4.8, and 8.4 GHz. We used the Multi Frequency Front Ends (Tan 1991)

in combination with the IVC+DZB back end[2] in continuum mode, with a bandwidth of 8×20 MHz. Gain and phase calibrations were performed with the calibrator 3C 286. The first observation at 4.8 GHz, 1.5 days after the burst, was reported as a non-detection with a 3σ upper limit of 261 μJy (van der Horst 2007b), but a careful reanalysis of the data resulted in a 3.7σ detection. The radio afterglow detection at ~ 5 days was reported by Chandra & Frail (2007) and van der Horst (2007a), using the Very Large Array at 8.64 GHz and the WSRT at 4.8 GHz respectively. The afterglow was bright enough to be detected up to 170 days after the burst at 4.8 GHz; after that, the flux dropped below the sensitivity limit. The measurement at 1.4 GHz resulted in a non-detection, while at 8.4 GHz we had a clear detection at 95 days after the burst. The details of our observations are shown in Table 1; the 4.8 GHz light curve is shown in Figure 3.

3. Data Analysis and Results

3.1. The Light Curve

The light curve (Figure 2) combines our optical, near-IR, and *Swift* data. The bands have been offset from their actual magnitudes for ease in reading. The original unextinguished magnitudes are listed in Table 1. Throughout this paper, we assume a standard flat cold dark matter cosmology (ΛCDM), with parameters $(\Omega_\Lambda, \Omega_\mathrm{M}, H_0) = (0.761, 0.239, 73\,\mathrm{km\,s^{-1}Mpc^{-1}})$, as found in the third-year WMAP data release (Spergel et al. 2007) assuming large-scale structure traced by luminous red galaxies (Tegmark et al. 2006). The particular set of values corresponds to the "Vanilla model" of Tegmark et al. (2006).

3.2. Fitting the Light Curve

Swift observations began 0.54 days after the burst, followed by ground-based observations beginning 0.8 days by the SARA telescope, closely followed by the rest of the various telescopes collected in this collaborative effort. Due to a lack of early coverage, it is not immediately clear whether or not there is a jet break. We fit a broken power-law decay to each band separately using the Beuermann function (Beuermann et al. 1999) as revised by Rhoads & Fruchter (2001):

[2]See §5.2 at http://www.astron.nl/wsrt/wsrtGuide/node6.html

$$F_\nu(t) = 2^{\frac{1}{n}} F_\nu(t_b) \left[\left(\frac{t}{t_b} \right)^{\alpha_1 n} + \left(\frac{t}{t_b} \right)^{\alpha_2 n} \right]^{-\frac{1}{n}}, \quad (1)$$

where F is the flux density in band ν, $F_\nu(tb)$ is the flux density in band ν at the break time, α_1 and α_2 are the slopes of the power-law decay (before and after the jet break, respectively), and n is the smoothness of the curve at the break.

The complicated shape of our light curve (see Figure 4) makes fitting the overall structure difficult. By using the flux at 2 days, we shifted all bands to the extinction-corrected R band for comparison and fitting. The entire data set is obviously not well-fit by a broken power-law function. Rapid flaring observed between one and two days post-trigger (§ 3.5), influences the fit. Broken power-law fits to the optical/UV/near-IR data set and the X-ray data set showed that this was indeed a poor model to the data set. In addition, this fit predicted that the afterglow would have been nearly a magnitude brighter than it was observed to be at 26.8 days. This would suggest the need for a second, non-standard jet break after 4 days.

By eliminating the flaring region between 1 and 2 days after the trigger, we can better constrain our fit. However, the best fit was determined by only considering the data taken after 2 days. At this point, it appears as if the flaring has settled to the point where the best estimate for the break time can be made. From the optical/UV/near-IR data set after 2 days, we determine an $\alpha_1 = 1.56 \pm 0.27$, $\alpha_2 = 2.47 \pm 0.13$, and a jet break time of $t = 3.73 \pm 0.52$ days. While the X-ray data do not require a break before 9 days, they are also not inconsistent with a break (see Table 2). Lack of an achromatic break is not an uncommon feature in Swift-era bursts (e.g., Curran et al. (2007)). The results of all of the fits to the optical/UV/near-IR and X-ray data can be found in Table 2.

Late-time MDM, LBT, and Chandra observations (Cenko et al. 2007b) were invaluable in the determination of a late jet break time, as were the numerous early observations which allowed us to resolve the early flaring activity so as not to be confused with a jet break. While the late MDM upper limit implied an optical jet break, the LBT detection at 26.8 days post-trigger confirmed the existence of a jet break. Second-epoch deep imaging of the field of GRB 070125 by the LBT did not result in the further detection of the source, thus allowing us to interpret the first detection as the afterglow (Dai et al. 2007). Late-time Chandra X-ray Telescope observations also imply a late jet break in the X-ray light curve. The Chandra upper limit of $2{\times}10^{-15}$ erg cm^{-2} s^{-1} (Cenko et al. 2007b) at 39.76 days after the burst was obtained in the 0.3 – 10 keV energy range, and is thus directly comparable to the XRT observations. Fits to the XRT data (Table 2) do not include this upper limit.

The fluence of the burst was measured independently by the Konus-Wind and RHESSI instruments. By extrapolating to the GRB rest-frame energy band of 1 keV – 10 MeV, we infer an isotropic energy of $E_{iso,Konus} = (9.44^{+0.40}_{-0.41}) \times 10^{53}$ erg and $E_{iso,RHESSI} = (8.27 \pm 0.39) \times 10^{53}$ erg (Bellm et al. 2007b). Assuming a jet break at $t = 3.73$ days and using the equations described in Sari et al. (1999), including a circumburst density of $n = 3$ cm^{-3} and a gamma-ray efficiency of $\eta_\gamma = 0.2$ (Bellm et al. 2007b), we find a jet half-opening angle of $\theta_{j,Konus} = 5.65^{+0.03}_{-0.03}$ degrees or $\theta_{j,RHESSI} = 5.74 \pm 0.04$ degrees. For a jet break time of 3.73 days, the corresponding collimated energy emission is $E_{\gamma,Konus} = 4.58^{+0.24}_{-0.25} \times 10^{51}$ erg, or $E_{\gamma,RHESSI} = (4.15 \pm 0.25) \times 10^{51}$ erg following Bloom et al. (2003).

Comprehensive broadband and energetics modeling of GRB 070125 was presented by Chandra et al. (2008). They derived a circumburst density of n $\sim$ 50 cm^{-3} from the kinetic energy and n = 15.7 cm^{-3} from a broadband fit using the synchrotron model. If we use n = 50 cm^{-3} to calculate E_γ, we find $E_{\gamma,Konus} = 9.26^{+0.49}_{-0.50} \times 10^{51}$ erg ($\theta_{j,Konus} = 8.03 \pm 0.04$ degrees); $E_{\gamma,RHESSI} = (8.39 \pm 0.50) \times 10^{51}$ erg ($\theta_{j,RHESSI} = 8.16 \pm 0.05$ degrees). Using the broadband fit n = 15.7 cm^{-3}, we derive $E_{\gamma,Konus} = 6.93^{0.37}_{0.38} \times 10^{51}$ erg ($\theta_{j,Konus} = 6.94 \pm 0.03$ degrees), $E_{\gamma,RHESSI} = (6.28 \pm 0.37) \times 10^{51}$ erg ($\theta_{j,RHESSI} = 7.07 \pm 0.04$ degrees). The most plausible value for the circumburst density comes from the broadband fit, so the energies derived from n = 15.7 will be quoted as the energy of the burst in this paper.

At $z = 1.547$, a jet break at 3.73 days (Figure 4) implies a rather large energy release (when placed in the context of the sample studied by Bloom et al. 2003). Both the observations of Konus-Wind and RHESSI imply that GRB 070125 is one of the most energetic bursts discovered to date (Bloom et al. 2003).

3.3. Spectral Energy Distribution

Due to the variable nature of the early-time light curve, special care was used in determining the SED. We used the method employed by Kann et al. (2006) for deriving the SED of GRB 030329. Using the R-band light curve as a reference, the other optical, UV, and near-IR bands were shifted until they matched the R-band light curve, which assumes the achromaticity already demonstrated above. Since we find no evidence for color evolution, use of the method is reasonable. The SED is then determined from the different colors, such as $U - R$. The R-band value is arbitrary, and thus also the absolute flux density scale of the SED. Also, due to achromaticity, no specific time should be associated with the SED shown in Figure 5. To model the intrinsic optical extinction, we use the three best-modeled extinction curves — those of the Milky Way (MW), Large Magellanic Cloud (LMC), and Small Magellanic Cloud (SMC) as parametrized by Pei (1992). We fit the SED with the

method described by Kann et al. (2006). The results are given in Table 3. We find a clear preference for the SMC dust model ($A_V = 0.11 \pm 0.04$ mag). This preference, as well as the intrinsic spectral slope β and the small host-galaxy extinction A_V, are all typical for the afterglows of (long) GRBs (e.g., Kann et al. 2006, 2007; Starling et al. 2007; Schady et al. 2007).

We combined the optical, UV, and near-IR photometry at, or extrapolated to, 4.26 days post-trigger with an X-ray spectrum extracted such that the log midpoint coincided with that of the optical SED described above. The *Swift* XRT X-ray spectrum was extracted using the method stated in § 2.1.1 and with the same extraction regions. The UVOT fluxes were obtained using the conversions in Poole et al. (2008). We calculated the transmission through the Lyman-α forest for each optical and UV band (e.g., Madau 1995) adopting the spectral slope $\beta = 0.58$ derived from the optical SED, and corrected for these factors: U transmission = 0.996, uvw1 = 0.848, uvm2 = 0.633, and uvw2 = 0.539. Galactic absorption and extinction were fixed at 4.8×10^{20} cm^{-2} (Dickey & Lockman 1990) and $E(B-V) = 0.052$ mag (Schlegel et al. 1998), respectively. The SED was created in count space following the method given by Starling et al. (2007), and having the advantage that no model for the X-ray data need be assumed *a priori*. We fit the SED using models consisting of an absorbed power law or absorbed broken power law with slopes free or tied to $\Gamma_1 = \Gamma_2 - 0.5$ as expected for a cooling break. X-ray absorption is modeled with the Xspec model *zphabs* and assuming solar metallicity.

We find that a broken power law provides a significantly better fit to the continuum than a single power law. The difference in slope between the two segments of the power law when both are left to vary tends to that expected for a cooling break: $\Delta\Gamma = 0.5$. Fixing the difference in the power-law slopes to 0.5 confirms this. (When compared to the single power law, the improvement in fit is significant according to the F-test, with probabilities of MW:10^{-6}, LMC:10^{-9}, and SMC:10^{-8}.) The cooling break can be well constrained to lie at 0.002 keV, 4.26 days since trigger. However, we caution that the distinction between the detection of a cooling break and a non-detection relies solely on the observed K-band flux, for which we have only two data points (see Table 1). Optical extinction is found to be $E(B-V) \approx 0.03$ mag (roughly equivalent to $A_V < 0.09$ mag), in full agreement with the fit from the optical SED alone. LMC and SMC extinction curves provide better fits than the MW extinction curve. The intrinsic X-ray absorption is relatively high, on the order of $N_{\rm H} \approx 2 \times 10^{21}$ cm^{-2}. Details of the fits are presented in Table 4. The unfolded SED and best-fitting model (BKNPL+LMC) are shown in Figure 5.

3.4. Light Curve and SED Analysis

The light curves at X-ray, UV, optical, and near-IR frequencies, and the SED spanning this large frequency range, can be utilized to determine the energy power-law index p of the electrons emitting the synchrotron radiation. Adopting the standard blast-wave model, the temporal and spectral indices, α and β (respectively), can be expressed in terms of p (Zhang & Mészáros 2004), assuming either a homogeneous or stellar wind-like circumburst medium. A single power-law fit to the X-ray light curve after the flare at 1.5×10^5 seconds results in a temporal index of $\alpha_X = 1.68^{+0.19}_{-0.15}$. For the analysis of the optical temporal slopes we take the fits without the flares (see Table 2), i.e., $\alpha_{\rm opt} = 1.56 \pm 0.27$ before the break and $\alpha_{\rm opt} = 2.47 \pm 0.13$ after the break.

The SED fits suggest that there is a cooling break at 0.002 keV (i.e. in the R band) 4.26 days after trigger. However, this result should be interpreted with caution, since there is no achromatic light-curve break across the optical bands observed and the K-band flux is the only one that discriminates between presence or absence of a cooling break in the optical regime. Furthermore, the value of p one can derive from the spectral slope above the tentative cooling break is $2\beta + 1 = 2.12 \pm 0.02$, which is not in agreement with the values one obtains from the X-ray temporal slope, $p = (4\alpha_{\rm X} + 2)/3 = 2.91^{+0.25}_{-0.20}$, and from the optical temporal slope in the case of a homogeneous circumburst medium, $p = (4\alpha_{\rm opt} + 3)/3 = 3.08 \pm 0.36$. If the circumburst medium is structured like a stellar wind, $p = (4\alpha_{\rm opt} + 1)/3 = 2.41 \pm 0.36$ from the optical temporal slope is in agreement with the spectral slope, but the X-ray temporal slope remains inconsistent. Such a discrepancy is not unprecedented (e.g., Perley et al. (2007)). However, we can derive an interpretation which is consistent with both the spectral and temporal fits (see below).

If one adopts the single power-law fit to the SED, all of the observed bands are either in between, or all of them are above, the peak frequency ν_m and cooling frequency ν_c. One then finds that $p = 2\beta + 1 = 2.98 \pm 0.02$ or $p = 2\beta = 1.98 \pm 0.02$, respectively.

If one assumes that $\nu_m < \nu_X < \nu_c$, p is equal to $(4\alpha_{\rm X} + 3)/3 = 3.24^{+0.25}_{-0.20}$ or $(4\alpha_{\rm X}X + 1)/3 = 2.57^{+0.25}_{-0.20}$, for a homogeneous or wind-like medium, respectively; if $\nu_m < \nu_c < \nu_X$, $p = (4\alpha_{\rm X}X + 2)/3 = 2.91^{+0.25}_{-0.20}$. Comparing these values for p with the ones from the single power-law SED fit, it is clear that they are only consistent for $\nu_m < \nu_X < \nu_c$ and a homogeneous medium.

The pre-break optical temporal slope results in values for p of $(4\alpha_{\rm opt} + 3)/3 = 3.08 \pm 0.36$ ($\nu_m < \nu_O < \nu_c$ and homogeneous medium), $(4\alpha_{\rm opt} + 1)/3 = 2.41 \pm 0.36$ ($\nu_m < \nu_O < \nu_c$ and stellar-wind medium), and $(4\alpha_{\rm opt} + 2)/3 = 2.75 \pm 0.36$ ($\nu_m < \nu_c < \nu_O$). Comparing these values for p with the values from the SED fit, again $\nu_m < \nu_O < \nu_c$ and a homogeneous

medium, which is the preferred situation from the X-ray temporal analysis, is consistent.

Concluding, the X-ray to infrared bands at ∼4 days are situated in between ν_m and ν_c, with $p \approx 3$ and the circumburst medium is homogeneous. We note that the p-value we derive for GRB 070125 lies at the high end of the observed distribution, and is similar to that measured for e.g. GRB 980519 (p=$2.96^{+0.06}_{-0.08}$, Starling et al. (2008)). Starling et al. (2008) showed that the p-distribution for a subsample of *BeppoSAX* GRBs is inconsistent with a single value of p for all bursts at the 3σ level, and constrain the intrinsic width of the parent distribution of p-values to $0.03 < \sigma_{\rm scat} < 1.40$ (3σ). A similar result was obtained for a *Swift* GRB subsample by Shen et al. (2006). If we adopt a mean observed p-value of 2.04, as measured for the BeppoSAX subsample, then p=3 lies within the expected observational scatter.

3.5. Rebrightening Episodes

From the light curve (Figure 2), we find evidence for two rebrightening or flaring episodes. These occur at $t = 1.15$ days (as observed by the Bok telescope, SARA, TNT, and KAIT) and $t = 1.36$ days (as observed by TNT and UVOT). The episode at $t = 1.15$ days is the best sampled, as illustrated by the Bok data in Figure 6. From the V band alone, we derive a change in magnitude of about 0.5 (corresponding to a 56% increase in flux) over a time period of $\Delta T \approx 8000$ s (0.093 days), or an average increase in flux density of 17.1 μJy/hour.

Rebrightening episodes are not an uncommon afterglow phenomenon, and have been attributed to a variety of causes, including density fluctuations in the external medium (clumps, turbulence, or wind-termination shock structures), energy injection episodes (refreshed shocks) from the catch-up of faster shells in the outflow, patchy shells leading to angular inhomogeneities, extended activity of the central engine, multi-component jets, or, in rare cases, microlensing; see the recent summary by Nakar & Granot (2007) for links to the original literature on these options. Nakar & Granot (2007) reconsidered the density fluctuation model with detailed numerical simulations, and find that sharp rebrightening episodes with $\Delta T/T < 1$ cannot be explained within this model. This result is in conflict with earlier conclusions, and the authors argue that their treatment of the reverse shock and photon travel-time effects explain the different outcome of their study.

The rebrightening episodes seen in GRB 070125 resemble those observed in GRB 021004 (de Ugarte Postigo et al. 2005; Pandey et al. 2003; Fox et al. 2003; Bersier et al. 2003; Uemura et al. 2003a), where three episodes with $\Delta T/T < 1$ are noted at $t \approx 0.05$, 0.8, and 2.6 days. The

preferred interpretation for these episodes is fluctuations in the energy surface density, i.e., a patchy-shell model (Granot & Königl 2003; Nakar & Oren 2004).

Another burst that lends itself to a comparison to GRB 070125 is the well-sampled "bumpy-ride" event GRB 030329. Late-time energy injection ("refreshed shocks") has been invoked to explain the "bumps" in this GRB (Granot et al. 2003). The well-resolved rebrightening episode discussed here is thus not likely caused by density fluctuations in the circumburst medium, but more likely attributed to angular or temporal energy fluctuations. Recently, Jóhannesson et al. (2006) presented a detailed analysis of relativistic fireballs with discrete or continuous energy injection, and showed that energy injection imprints significant features on the afterglow, and thus provides a valuable diagnostic tool to study GRB fireball physics beyond the single-explosion standard model. In particular, Jóhannesson et al. (2006) find that refreshed shocks from a discrete injection episode at $t = 1.4$ days (with an energy twice that of the initial energy injection) may, if not delivered uniformly across the shock surface (i.e., if a patchy shell is assumed), explain the sharp bump at $t = 3.5$ days observed in GRB 000301C. A more detailed follow-up paper is planned to further explore the rebrightening episodes found in GRB 070125.

3.6. Radio Light Curve

The WSRT light curve at 4.8 GHz (see Figure 3) displays the typical radio afterglow light-curve characteristics (e.g., Frail et al. 1997; Sari 1998). Except for the first measurement, all the observations were performed after the jet-break time we derived from the optical light curves. At early times, the radio bands are situated below the synchrotron self-absorption frequency ν_a and the peak frequency ν_m. Since these two characteristic frequencies move to lower observing frequencies in time, the light curve first rises up to the jet break, after which the flux remains constant. The measurements at 1.5 and 5.6 days seem to deviate from this behavior, but this can be explained by the effect of radio scintillation (Goodman 1997). The rise in flux after ~ 40 days is caused by the passage of ν_m through the observing band, and the turnover at ~ 90 days by the passage of ν_a, after which the light curve declines quite steeply with a temporal index equal to the electron energy power-law index $p \approx 3$. More detailed modeling of the radio light curve will be presented in a follow-up paper.

3.7. Spectroscopy

It is evident from Figure 7 that the spectrum taken on Jan 26, 2007 at 05:44:05 is nearly featureless. We have convolved the spectrum with a Gaussian matched to the instrumental resolution, and derive a 4σ equivalent width limits of approximately 10 Å at 3100 Å, 5 Å at 3200 Å, 3 Å at 3400 Å, 1.5 Å at 4000 Å, and 1 Å redward of 6000 Å. We identify only a few features at 4σ statistical significance[3] as listed in Table 5.

Cenko et al. (2007a) have reported the detection of a relatively weak Mg II doublet ($W_{MgII} < 1$ Å) in their afterglow spectrum of GRB 070125, leading to an implied redshift of 1.547. Our spectra do not confirm this line measurement, but the reported equivalent width lies below our detection threshold. However, we identify a strong feature at 3947.1 Å which corresponds to the expected position of the C IV doublet for $z = 1.547$. C^{+3} gas is frequently associated with Mg II absorbers (Churchill et al. 2000) and also gas surrounding GRB host galaxies (e.g., Mirabal et al. 2003). Unfortunately, we lack the spectral resolution to resolve the C IV doublet, but the likelihood of a misidentification is very low given the paucity of absorption lines in our data set. Furthermore, we observe weak absorption at the expected position of the Si IV doublet for $z = 1.547$ which is spectrally resolved (Figure 7) but has less than 4σ statistical significance. Altogether, the spectrum provides strong evidence for a metal-line absorption system at $z = 1.547$, especially given the independent report of Mg II absorption by Fox et al. (2007). In turn, we establish this redshift as the lowest possible value for GRB 070125.

Of principal interest to our study is whether this metal-line absorption system results from gas in the GRB host galaxy and therefore establishes the redshift of GRB 070125. There are two indisputable signatures that an absorption system corresponds to a GRB host galaxy. (1) One observes fine-structure levels of O^0, Si^+, or Fe^+. These transitions, which have never been detected in an intervening system with quasar absorption-line spectroscopy, are known to arise from indirect radiative pumping by the GRB afterglow (Prochaska et al. 2006a; Vreeswijk et al. 2007). (2) One positively identifies the Lyα forest imprint of the intergalactic medium and associates the highest redshift Lyα absorption with the GRB. In this latter case, one frequently observes a damped Lyα (DLA) profile[4] at the GRB redshift (Jakobsson et al. 2006).

Our spectrum reveals neither of these two signatures. First, we note no significant ab-

[3]Note that systematic errors (e.g., continuum fitting) imply that the true significance limit is approximately 3σ.

[4]H I column density $N_{\rm HI} > 2 \times 10^{20}\,{\rm cm}^{-2}$.

sorption from even the resonance lines of O^0, Si^+, or Fe^+, and we place relatively stringent upper limits on their equivalent widths (Table 5). Second, our spectrum does not unambiguously show the Lyα forest. Figure 8 presents the spectral region at $\lambda < 3400$ Å. Overplotted on the data (green line) is a DLA profile centered at $z = 1.547$ assuming $N_{\rm HI} = 10^{20.3}\,{\rm cm}^{-2}$. Although the data formally reject the presence of a DLA system at this redshift, we caution that systematic effects (wavelength calibration, continuum placement) are not sufficiently large at $\lambda < 3100$ Å to rule out a DLA profile at $> 99\%$ c.l. The data do, however, rule out a DLA profile at all wavelengths greater than 3140 Å.

The absence of a strong DLA system or an obvious series of Lyα absorption lines (i.e., the Lyα forest) places an upper limit on the redshift of GRB 070125. A reasonable estimate is to designate the absorption line (presently unidentified) at $\lambda = 3375$ Å as a Lyα transition and set $z_{GRB} \leq 1.78$. The identification of this feature as Lyα is not supported by any coincident metal-line absorption (e.g., C IV). Furthermore, the implied rest equivalent width, $W_{Ly\alpha} = 1.4$ Å, would be significantly lower than any thus far reported for gas surrounding a GRB. Nevertheless, we cannot rule out this interpretation altogether. Applying Occam's razor to our full set of observations, we associate the metal-line absorption system at $z = 1.547$ with the host galaxy of GRB 070125. To date, every absorption system which has been unambiguously associated with a GRB host galaxy (i.e., using the criteria above) has shown strong Lyα, Mg II, and C IV absorption. In fact, this afterglow spectrum would already represent the weakest Mg II doublet ever reported, although weaker C IV equivalent widths exist (Shin et al. 2006).

Whether or not we associate the $z = 1.547$ metal-line system with GRB 070125, this afterglow spectrum is remarkable in several respects. First, it is evident that the H I column density is low. Taking $z_{GRB} = 1.547$, we have argued that the data prefer $N_{\rm HI} < 10^{20.3}\,{\rm cm}^{-2}$, which is a rare but not unprecedented result (Fynbo et al. 2005; Prochaska et al. 2005, 2006a). If $z > 1.547$, then the Lyα transition has the lowest equivalent width reported for a GRB. Either way, the low $N_{\rm HI}$ value is remarkable given the expectation that the GRB progenitor arises in a high density, star-forming region. Similar cases are discussed in Watson et al. (2007). Second, even taking $z_{GRB} = 1.547$ the C IV, Mg II, and other low-ion equivalent widths are among the lowest observed to date for gas surrounding a GRB. Unfortunately, it is difficult to estimate the gas metallicity without a meaningful constraint on the $N_{\rm HI}$ value. Adopting $N_{\rm HI} = 10^{19}\,{\rm cm}^{-2}$, the upper limit to the equivalent width of Mg II λ2796 implies a Mg/H ratio less than 1/10 the solar value. We derive a similar value adopting the upper limit to the equivalent width of Si II 1526 ($W_{1526}^{rest} < 0.5$ Å) and assuming the metallicity/W_{1526} relation of Prochaska et al. (2008).

Taking both the spectroscopy and SED results into consideration, the host-galaxy prop-

erties of GRB 070125 are consistent with those found in the sample presented by Fruchter et al. (2006).

4. Implications and Conclusions

While we do not have data before 0.545 days (the first exposures were obtained in V with the UVOT), sampling thereafter is reasonably dense in time (see Figure 2), until about 4 days after T_0. These observations suggest a possible jet break in the 1–3 day window. However, the strong variability (rebrightening episodes) around $t \approx 1$–2 days interferes with a clean detection of the jet break, and it is conceivable that the actual afterglow light curve is not best represented by a broken power law (the Beuermann-like profile) with superimposed "flares," but instead by three or more power laws, interrupted and perhaps re-established by several periods of rebrightening. GRB 030329 provides an example of a GRB with a jet break at $t \approx 0.5$ days (Uemura et al. 2003b; Price et al. 2003), followed by multiple rebrightening episodes during subsequent days (e.g. Greiner et al. 2003; Lipkin et al. 2004). Given that the light curve of GRB 070125 exhibits strong variability, a jet-break interpretation requires extreme care. However, the sparse late-time data do suggest that a break has occurred. Fitting the data past 2 days indicates that the actual jet break is more likely to be identified with the required change in slope at $t = 3.7$ days. If there indeed was no very early break in the optical power-law decay (before 0.5 days) and this late break time established from our fits is to be identified with the jet break, the indicated jet half-opening angle of 6.94° implies $E_\gamma = 6.93 \times 10^{51}$ erg (from $E_{iso,Konus}$), and GRB 070125 is consistent with the Ghirlanda relation (Ghirlanda et al. 2004).

The redshift allows us to place GRB 070125 in general context. Figure 9 shows the intrinsic afterglow of GRB 070125 in comparison with 52 other afterglows from the samples of Kann et al. (2006) and Kann et al. (2007). These afterglows are in the R band and have been corrected for Galactic extinction and, where possible, for host galaxy and supernova contributions. The afterglow of GRB 070125 was constructed by shifting BVI data to the R band, as only BV data are available at early times. Using the method described by Kann et al. (2006), all afterglows have been corrected for rest-frame extinction and shifted to a common redshift of 1, allowing a direct comparison. The afterglow of GRB 070125 is found to be among the most luminous afterglows; at the time of the rebrightening at one day, only the afterglow of GRB 021004 is brighter. The afterglow properties thus corroborate the inferences we made in the previous section, where the beaming-corrected burst energy in the 1–10,000 keV regime (Bellm et al. 2007a) was found to be on the high side of the observed statistical distribution.

Had GRB 070125 been much nearer, it would have given us an unprecedented opportunity to observe an afterglow on a much longer time scale, detect the additional emissions from an associated supernova, and possibly revealed a host galaxy. At a redshift of 1.547, an unextinguished SN 1998bw would have peaked at $R \approx 27$ mag about one month after the burst. The LBT detection at late times could be explained with a supernova like SN 1998bw, if one allows a scaling factor of $k = 2.25$, which is significantly larger than indicated by the properties of the sample of established GRB-supernovae (Zeh et al. 2005; Ferrero et al. 2006). Additionally, assuming that the late-time detection is composed entirely of supernova emission implies an even steeper afterglow decay. Given the uncertainties when extrapolating the light-curve properties of SN 1998bw to a redshift of 1.5, we caution that this factor has a large uncertainty. Based on what is known so far about the luminosities of GRB-SNe (Zeh et al. 2004; Ferrero et al. 2006), it seems unlikely that the LBT data point is indeed representing SN light. Another alternative is light from an underlying host galaxy (not discernible in the images). Due to the second-epoch non-detection by the LBT (Dai et al. 2007), we can conclude that the host galaxy must be fainter than $M_V = 18.2$ mag ($R > 26.1$ mag), which is comparable to the Magellanic Clouds or even fainter (van den Bergh 2000), but consistent with the distribution found in the *Hubble Space Telescope* survey by Fruchter et al. (2006). The low metallicity we inferred from the spectra would also be consistent with a small, low-luminosity host galaxy.

GRB 070125 was unusual in several aspects. It had at least two sharp rebrightening episodes, it was intrinsically bright, and did not reveal the often associated DLA and Mg II features in its smooth spectrum. The collective efforts of a large group allowed us to learn much about this burst, but it also provides a good example of the all-too-common situation that the world resources are too scarce to follow every burst with the kind of intensity in time and bandpass that may be required to extract enough information about each burst. Bumps have to be resolved, light curves need to be followed over longer time scales with greater sampling frequency, SEDs need to be established at many epochs, the associated supernovae should be checked even if the redshift is large, and host-galaxy properties should be established. Global coverage is necessary so that bumps and jet breaks are not missed, especially if future mission, such as EXIST (Grindlay & The Exist Team 2006), may result in much higher burst rates.

A.C.U. and D.H.H. would like to thank Martha Leake and Matt Wood for generously sharing their SARA time with us. J.R.T. would like to acknowledge support from NSF grant AST-0307413. D.A.K. and S.K. were supported by DFG grant Kl 766/13-2. J.P.H. acknowledges support from Swift Guest Investigator Grant NNG06GJ25G. The work of P.W.A.R., D.N.B., and J.L.R. was sponsored at Penn State University by NASA contract NAS5-00136.

Observations reported here were in part obtained at the MMT Observatory, a joint facility of the University of Arizona and the Smithsonian Institution. J.D., W.Z, and Y.Q. are supported by NSFC Grant No. 10673014. E.M. and E.P. are members of the Collaborazione Italiana Burst Ottici (CIBO) and thank the staff astronomers of the TNG for the excellent support. Effort by C.W.H. was supported by a grant from NASA's Planetary Astronomy Program. R.L.C.S. acknowledges support from STFC. K.C.H. is grateful for IPN support under NASA grants NNG06GE69G and NNX06AI36G, and under JPL Contract 128043. The Westerbork Synthesis Radio Telescope is operated by ASTRON (Netherlands Foundation for Research in Astronomy) with support from the Netherlands Foundation for Scientific Research (NWO). A.J.v.d.H. was supported by an appointment to the NASA Postdoctoral Program at NSSTC, administered by Oak Ridge Associated Universities through a contract with NASA. A.V.F.'s group at UC Berkeley is supported by NSF grant AST–0607485, NASA/Swift grant NNG06GI86G, the TABASGO Foundation, and the Sylvia and Jim Katzman Foundation. Some of the data presented herein were obtained at the W. M. Keck Observatory, which is operated as a scientific partnership among the California Institute of Technology, the University of California and NASA. The Observatory was made possible by the generous financial support of the W. M. Keck Foundation.

REFERENCES

Amati, L. 2006, MNRAS, 372, 233

Barthelmy, S. D., et al. 2005, Space Science Reviews, 120, 143

Bellm, E., Bandstra, M., Boggs, S., Wigger, C., Hajdas, W., Smith, D. M., & Hurley, K. 2007, GRB Coordinates Network, 6025, 1

Bellm, E. C., et al. 2007, ArXiv e-prints, 710, arXiv:0710.4590

Berger, E., Penprase, B. E., Cenko, S. B., Kulkarni, S. R., Fox, D. B., Steidel, C. C., & Reddy, N. A. 2006, ApJ, 642, 979

Bersier, D., et al. 2003, ApJ, 584, L43

Bessell, M. S. 1979, PASP, 91, 589

Beuermann, K., et al. 1999, A&A, 352, L26

Bloom, J. S., Starr, D., & Blake, C. H. 2007, GRB Coordinates Network, 6054, 1

Bloom, J. S., Frail, D. A., & Kulkarni, S. R. 2003, ApJ, 594, 674

Bromm, V., & Loeb, A. 2006, ApJ, 642, 382

Burrows, D. N., & Racusin, J. 2007, GRB Coordinates Network, 6181, 1

Burrows, D. N., et al. 2005, Space Science Reviews, 120, 165

Cardelli, J. A. 1994, Science, 265, 209

Cardelli, J. A., Clayton, G. C., & Mathis, J. S. 1989, Interstellar Dust, 135, 5P

Cardelli, J. A., Clayton, G. C., & Mathis, J. S. 1989, ApJ, 345, 245

Cenko, S. B., et al. 2007, ArXiv e-prints, 712, arXiv:0712.2828

Cenko, S. B., & Fox, D. B. 2007, GRB Coordinates Network, 6028, 1

Cenko, S. B. 2007, GRB Coordinates Network, 6034, 1

Cenko, S. B., Soderberg, A. M., Frail, D. A., & Fox, D. B. 2007, GRB Coordinates Network, 6186, 1

Chandra, P., Chandra, I., & Gupta, N. 2007, GRB Coordinates Network, 6102, 1

Chandra, P., Bock, D., Soderberg, A. M., Frail, D. A., & Kulkarni, S. R. 2007, GRB Coordinates Network, 6073, 1

Chandra, P., & Frail, D. A. 2007, GRB Coordinates Network, 6061, 1

Christensen, L., Hjorth, J., & Gorosabel, J. 2004, A&A, 425, 913

Churchill, C. W., Mellon, R. R., Charlton, J. C., Jannuzi, B. T., Kirhakos, S., Steidel, C. C., & Schneider, D. P. 2000, ApJ, 543, 577

Costa, E., et al. 1997, Nature, 387, 783

Curran, P. A., et al. 2007, MNRAS, 381, L65

Dai, X., et al. 2007, ArXiv e-prints, 712, arXiv:0712.2239

de Ugarte Postigo, A., et al. 2005, A&A, 443, 841

Della Valle, M., et al. 2006, Nature, 444, 1050

Deng, J., & Zheng, W. 2006, Il Nuovo Cimento B, 121, 1469

Dickey, J. M., & Lockman, F. J. 1990, ARA&A, 28, 215

Durig, D. T. 2007, GRB Coordinates Network, 6051, 1

Durig, D. T., & Gary, B. 2007, GRB Coordinates Network, 6048, 1

Fan, X., Carilli, C. L., & Keating, B. 2006, ARA&A, 44, 415

Ferrero, P., et al. 2006, A&A, 457, 857

Filippenko, A. V., Li, W. D., Treffers, R. R., & Modjaz, M. 2001, in Small Telescope Astronomy on Global Scales, ed. W. P. Chen, C. Lemme, & B. Paczyński (San Francisco: ASP, Conf. Ser. Vol. 246), 121

Filippenko, A. V. 1997, ARA&A, 35, 309

Fox, D. B., Berger, E., Price, P. A., & Cenko, S. B. 2007, GRB Coordinates Network, 6071, 1

Fox, D. W., et al. 2003, Nature, 422, 284

Frail, D. A., et al. 2001, ApJ, 562, L55

Frail, D. A., Kulkarni, S. R., Nicastro, L., Feroci, M., & Taylor, G. B. 1997, Nature, 389, 261

Fruchter, A. S., et al. 2006, Nature, 441, 463

Fynbo, J. P. U., et al. 2005, ApJ, 633, 317

Fynbo, J. P. U., et al. 2006, Nature, 444, 1047

Galama, T. J., et al. 1998, Nature, 395, 670

Gal-Yam, A., et al. 2006, ApJ, 639, 331

Gallerani, S., Salvaterra, R., Ferrara, A., & Choudhury, T. R. 2007, ArXiv e-prints, 710, arXiv:0710.1303

Garnavich, P., et al. 2007, GRB Coordinates Network, 6165, 1

Gehrels, N., et al. 2006, ArXiv Astrophysics e-prints, arXiv:astro-ph/0610635

Gehrels, N. 2004, New Astronomy Review, 48, 431

Gehrels, N., et al. 2004, ApJ, 611, 1005

Ghirlanda, G., Ghisellini, G., & Lazzati, D. 2004, ApJ, 616, 331

Golenetskii, S., Aptekar, R., Mazets, E., Pal'Shin, V., Frederiks, D., & Cline, T. 2007, GRB Coordinates Network, 6049, 1

Goodman, J. 1997, New Astronomy, 2, 449

Graham, J. A. 1982, PASP, 94, 244

Granot, J., & Königl, A. 2003, ApJ, 594, L83

Granot, J., Nakar, E., & Piran, T. 2003, Nature, 426, 138

Greco, G., et al. 2007, GRB Coordinates Network, 6047, 1

Greiner, J., et al. 2003, Nature, 426, 157

Greiner, J., et al. 2007, GRB Coordinates Network, 6449, 1

Grindlay, J. E., & The Exist Team 2006, Gamma-Ray Bursts in the Swift Era, 836, 631

Haislip, J., Reichart, D., Lacluyze, A., Ivarsen, K., Nysewander, M., Foster, A., & Crain, J. A. 2007, GRB Coordinates Network, 6044, 1

Haislip, J. B., et al. 2006, Nature, 440, 181

Hiltner, W. A. 1964, Astronomical Techniques, University of Chicago Press, Chicago, IL

Hjorth, J., et al. 2003, Nature, 423, 847

Hurley, K., et al. 2007, GRB Coordinates Network, 6024, 1

Jakobsson, P., et al. 2006, A&A, 447, 897

Jóhannesson, G., Björnsson, G., & Gudmundsson, E. H. 2006, ApJ, 647, 1238

Jordi, K., Grebel, E. K., & Ammon, K. 2006, A&A, 460, 339

Kaneko, Y., Preece, R. D., Briggs, M. S., Paciesas, W. S., Meegan, C. A., & Band, D. L. 2006, ApJS, 166, 298

Kann, D. A., et al. 2007, ArXiv e-prints, 712, arXiv:0712.2186

Kann, D. A., Klose, S., & Zeh, A. 2006, ApJ, 641, 993

Kawai, N., et al. 2006, Nature, 440, 184

Klebesadel, R. W., Strong, I. B., & Olson, R. A. 1973, ApJ, 182, L85

Kouveliotou, C., Meegan, C. A., Fishman, G. J., Bhat, N. P., Briggs, M. S., Koshut, T. M., Paciesas, W. S., & Pendleton, G. N. 1993, ApJ, 413, L101

Kuin, N. P. M., & Rosen, S. R. 2008, MNRAS, 383, 383

Le Floc'h, E., Charmandaris, V., Forrest, W. J., Mirabel, I. F., Armus, L., & Devost, D. 2006, ApJ, 642, 636

Li, W., Filippenko, A. V., Chornock, R., & Jha, S. 2003, PASP, 115, 844

Li, W., Jha, S., Filippenko, A. V., Bloom, J. S., Pooley, D., Foley, R. J., & Perley, D. A. 2006, PASP, 118, 37

Lipkin, Y. M., et al. 2004, ApJ, 606, 381

Madau, P. 1995, ApJ, 441, 18

Malesani, D., et al. 2004, ApJ, 609, L5

Marshall, F. E., vanden Berk, D. E., & Racusin, J. 2007, GRB Coordinates Network, 6041, 1

McQuinn, M., Lidz, A., Zaldarriaga, M., Hernquist, L., & Dutta, S. 2007, ArXiv e-prints, 710, arXiv:0710.1018

Metzger, M. R., Djorgovski, S. G., Kulkarni, S. R., Steidel, C. C., Adelberger, K. L., Frail, D. A., Costa, E., & Frontera, F. 1997, Nature, 387, 878

Mirabal, N., Halpern, J., & Thorstensen, J. R. 2007, GRB Coordinates Network, 6096, 1

Mirabal, N., Halpern, J. P., An, D., Thorstensen, J. R., & Terndrup, D. M. 2006, ApJ, 643, L99

Mirabal, N., et al. 2003, ApJ, 595, 935

Nakar, E., & Granot, J. 2007, MNRAS, 380, 1744

Nakar, E., & Oren, Y. 2004, ApJ, 602, L97

Oke, J. B., et al. 1995, PASP, 107, 375

Pandey, S. B., et al. 2003, Bulletin of the Astronomical Society of India, 31, 19

Pei, Y. C. 1992, ApJ, 395, 130

Perley, D. A., et al. 2007, ArXiv Astrophysics e-prints, arXiv:astro-ph/0703538

Pian, E., et al. 2006, Nature, 442, 1011

Poole, T. S., et al. 2008, MNRAS, 383, 627

Price, P. A., et al. 2003, Nature, 423, 844

Prochaska, J. X., Chen, H.-W., Wolfe, A. M., Dessauges-Zavadsky, M., & Bloom, J. S. 2008, ApJ, 672, 59

Prochaska, J. X., Foley, R., Tran, H., Bloom, J. S., & Chen, H.-W. 2006, GRB Coordinates Network, 4593, 1

Prochaska, J. X., Chen, H.-W., & Bloom, J. S. 2006, ApJ, 648, 95

Prochaska, J. X., Foley, R. J., Chen, H.-W., Bloom, J. S., Hurley, K., Cooper, M., Guhathakurta, R., & Li, W. 2005, GRB Coordinates Network, 3971, 1

Racusin, J. L., Cummings, J., Marshall, F. E., Burrows, D. N., Krimm, H., & Sato, G. 2007, GCNR, 28, 3 (2007), 28, 3

Racusin, J., Cummings, J., & Marshall, F. E. 2007, GCNR, 28, 2 (2007), 28, 2

Racusin, J., Cummings, J., & Marshall, F. 2007, GCNR, 28, 1 (2007), 28, 1

Racusin, J., & Vetere, L. 2007, GRB Coordinates Network, 6030, 1

Rhoads, J. E., & Fruchter, A. S. 2001, ApJ, 546, 117

Roming, P. W. A., et al. 2005, Space Science Reviews, 120, 95

Sari, R. 1998, ApJ, 494, L49

Sari, R., Piran, T., & Halpern, J. P. 1999, ApJ, 519, L17

Savaglio, S. 2006, New Journal of Physics, 8, 195

Schady, P., et al. 2007, MNRAS, 377, 273

Schlegel, D. J., Finkbeiner, D. P., & Davis, M. 1998, ApJ, 500, 525

Shen, R., Kumar, P., & Robinson, E. L. 2006, MNRAS, 371, 1441

Shin, M.-S., et al. 2006, ArXiv Astrophysics e-prints, arXiv:astro-ph/0608327

Spergel, D. N., et al. 2007, ApJS, 170, 377

Spergel, D. N., et al. 2003, ApJS, 148, 175

Stanek, K. Z., et al. 2003, ApJ, 591, L17

Starling, R. L. C., van der Horst, A. J., Rol, E., Wijers, R. A. M. J., Kouveliotou, C., Wiersema, K., Curran, P. A., & Weltevrede, P. 2008, ApJ, 672, 433

Starling, R. L. C., Wijers, R. A. M. J., Wiersema, K., Rol, E., Curran, P. A., Kouveliotou, C., van der Horst, A. J., & Heemskerk, M. H. M. 2007, ApJ, 661, 787

Tan, G. H. 1991, IAU Colloq. 131: Radio Interferometry. Theory, Techniques, and Applications, 19, 42

Tegmark, M., et al. 2006, Phys. Rev. D, 74, 123507

Terra, F., et al. 2007, GRB Coordinates Network, 6064, 1

Totani, T., Kawai, N., Kosugi, G., Aoki, K., Yamada, T., Iye, M., Ohta, K., & Hattori, T. 2006, PASJ, 58, 485

Totani, T., Kawai, N., Kosugi, G., Aoki, K., Yamada, T., Iye, M., Ohta, K., & Hattori, T. 2007, Highlights of Astronomy, 14, 265

Uemura, M., Arai, A., & Uehara, T. 2007, GRB Coordinates Network, 6039, 1

Uemura, M., Kato, T., Ishioka, R., & Yamaoka, H. 2003, PASJ, 55, L31

Uemura, M., et al. 2003, Nature, 423, 843

Updike, A. C., Hartmann, D. H., Bryngelson, G. L., Goldthwaite, R. C., & Puls, J. R. 2007, GRB Coordinates Network, 6029, 1

van den Bergh, S. 2000, Cambridge Astrophysics Series, 35,

van der Horst, A. J. 2007, GRB Coordinates Network, 6063, 1

van der Horst, A. J. 2007, GRB Coordinates Network, 6042, 1

van Paradijs, J., et al. 1997, Nature, 386, 686

Vreeswijk, P. M., et al. 2007, A&A, 468, 83

Watson, D., Hjorth, J., Fynbo, J. P. U., Jakobsson, P., Foley, S., Sollerman, J., & Wijers, R. A. M. J. 2007, ApJ, 660, L101

Williams, G. G., Olszewski, E., Lesser, M. P., & Burge, J. H. 2004, Proc. SPIE, 5492, 787

Wolf, C., & Podsiadlowski, P. 2007, MNRAS, 375, 1049

Woosley, S. E., & Bloom, J. S. 2006, ARA&A, 44, 507

Xing, L. P., Zhai, M., Qiu, Y. L., Wei, J. Y., Hu, J. Y., Deng, J. S., Urata, Y., & Zheng, W. K. 2007, GRB Coordinates Network, 6035, 1

Yamaoka, K., et al. 2005, Nuclear Science, IEEE Transactions on, 52, 2765

Yoshida, M., Yanagisawa, K., & Kawai, N. 2007, GRB Coordinates Network, 6050, 1

Zeh, A., Kann, D. A., Klose, S., & Hartmann, D. H. 2005, Nuovo Cimento C Geophysics Space Physics C, 28, 617

Zeh, A., Klose, S., & Hartmann, D. H. 2004, ApJ, 609, 952

Zhang, B., & Mészáros, P. 2004, International Journal of Modern Physics A, 19, 2385

Table 1. OBSERVATIONAL CAMPAIGN

Time	Mag or Flux	Error	Instrument	Band
1.517	203	5.5E-5	WSRT	4.8 GHz
5.642	102	2.6E-5	WSRT	4.8 GHz
8.634	241	2.6E-5	WSRT	4.8 GHz
12.929	220	2.6E-5	WSRT	4.8 GHz
13.927	-25.0	6.3E-5	WSRT	1.4 GHz
17.916	222	2.7E-5	WSRT	4.8 GHz
34.854	196	3.0E-5	WSRT	4.8 GHz
50.827	240	4.5E-5	WSRT	4.8 GHz
85.730	318	4.9E-5	WSRT	4.8 GHz
95.703	450	1.0E-4	WSRT	8.4 GHz
170.499	157	5.2E-5	WSRT	4.8 GHz
278.204	126	7.9E-5	WSRT	4.8 GHz
1.349	19.25	0.10	UVOT	uvw2
1.416	19.14	0.10	UVOT	uvw2
1.484	19.41	0.11	UVOT	uvw2
1.749	19.51	0.15	UVOT	uvw2
1.816	19.44	0.15	UVOT	uvw2
1.883	19.92	0.18	UVOT	uvw2
1.950	19.59	0.16	UVOT	uvw2
2.017	20.33	0.21	UVOT	uvw2
2.085	19.77	0.17	UVOT	uvw2
2.149	19.90	0.18	UVOT	uvw2
2.252	20.61	0.18	UVOT	uvw2
2.285	19.75	0.18	UVOT	uvw2
2.521	20.54	0.17	UVOT	uvw2
2.723	20.42	0.17	UVOT	uvw2
2.929	20.79	0.18	UVOT	uvw2
3.297	20.95	0.16	UVOT	uvw2
3.525	20.97	0.17	UVOT	uvw2
4.157	21.68	0.12	UVOT	uvw2
1.360	18.91	0.11	UVOT	uvm2
1.427	19.13	0.14	UVOT	uvm2
1.492	19.31	0.24	UVOT	uvm2
1.755	19.41	0.20	UVOT	uvm2
1.822	19.28	0.20	UVOT	uvm2
1.889	19.64	0.23	UVOT	uvm2
1.956	19.27	0.21	UVOT	uvm2

Table 1—Continued

Time	Mag or Flux	Error	Instrument	Band
2.023	19.82	0.26	UVOT	uvm2
2.090	19.76	0.25	UVOT	uvm2
2.155	19.62	0.24	UVOT	uvm2
2.290	20.68	0.26	UVOT	uvm2
2.627	20.55	0.37	UVOT	uvm2
3.101	21.03	0.23	UVOT	uvm2
2.425	20.28	0.34	UVOT	uvm2
2.491	20.00	0.25	UVOT	uvm2
2.626	20.49	0.30	UVOT	uvm2
4.098	21.58	0.23	UVOT	uvm2
1.337	18.92	0.11	UVOT	uvw1
1.404	19.33	0.13	UVOT	uvw1
1.473	19.02	0.12	UVOT	uvw1
1.743	19.27	0.17	UVOT	uvw1
1.810	19.45	0.19	UVOT	uvw1
1.910	19.50	0.14	UVOT	uvw1
2.110	20.18	0.17	UVOT	uvw1
2.313	19.95	0.17	UVOT	uvw1
2.515	20.26	0.18	UVOT	uvw1
2.716	20.18	0.17	UVOT	uvw1
3.123	20.66	0.12	UVOT	uvw1
2.279	19.53	0.20	UVOT	uvw1
4.049	21.09	0.11	UVOT	uvw1
1.340	18.81	0.10	UVOT	U
1.408	18.83	0.10	UVOT	U
1.476	18.81	0.10	UVOT	U
1.745	19.19	0.14	UVOT	U
1.845	19.85	0.13	UVOT	U
1.879	19.46	0.16	UVOT	U
1.946	19.65	0.17	UVOT	U
2.246	20.28	0.10	UVOT	U
2.517	20.03	0.13	UVOT	U
2.854	20.69	0.09	UVOT	U
3.487	20.85	0.08	UVOT	U
0.555	18.66	0.03	UVOT	B
0.622	18.95	0.04	UVOT	B
0.689	18.92	0.04	UVOT	B

Table 1—Continued

Time	Mag or Flux	Error	Instrument	Band
0.857	19.69	0.05	PROMPT	B
0.947	19.70	0.04	PROMPT	B
1.034	19.76	0.01	Bok	B
1.035	19.72	0.01	Bok	B
1.037	19.71	0.01	Bok	B
1.038	19.73	0.02	Bok	B
1.040	19.71	0.01	Bok	B
1.041	19.73	0.01	Bok	B
1.042	19.71	0.01	Bok	B
1.044	19.69	0.01	Bok	B
1.343	19.92	0.09	UVOT	B
1.410	19.85	0.09	UVOT	B
1.478	19.49	0.08	UVOT	B
1.813	20.12	0.07	UVOT	B
2.316	20.89	0.05	UVOT	B
3.187	21.06	0.04	UVOT	B
4.651	22.31	0.22	TNG	B
0.545	18.37	0.05	UVOT	V
0.611	18.66	0.05	UVOT	V
0.679	18.66	0.05	UVOT	V
0.736	18.80	0.05	UVOT	V
0.802	19.15	0.07	SARA	V
0.821	18.95	0.04	SARA	V
0.889	19.33	0.05	SARA	V
0.891	19.21	0.02	PROMPT	V
0.914	19.15	0.05	SARA	V
0.935	19.23	0.04	SARA	V
0.957	19.28	0.04	SARA	V
0.967	19.14	0.04	PROMPT	V
0.981	19.21	0.04	SARA	V
1.007	19.33	0.03	SARA	V
1.046	19.20	0.01	Bok	V
1.049	19.15	0.01	Bok	V
1.051	19.15	0.01	Bok	V
1.052	19.15	0.01	Bok	V
1.054	19.15	0.02	Bok	V
1.055	19.16	0.01	Bok	V

Table 1—Continued

Time	Mag or Flux	Error	Instrument	Band
1.056	19.17	0.01	Bok	V
1.058	19.15	0.02	Bok	V
1.059	19.14	0.02	Bok	V
1.063	18.88	0.05	SARA	V
1.063	19.13	0.01	Bok	V
1.066	19.12	0.01	Bok	V
1.071	19.06	0.04	SARA	V
1.078	19.05	0.04	SARA	V
1.083	19.07	0.01	Bok	V
1.084	19.08	0.01	Bok	V
1.087	19.06	0.01	Bok	V
1.088	19.20	0.05	SARA	V
1.088	19.04	0.01	Bok	V
1.090	19.05	0.01	Bok	V
1.091	19.04	0.01	Bok	V
1.094	19.02	0.01	Bok	V
1.095	19.03	0.01	Bok	V
1.097	19.04	0.01	Bok	V
1.098	19.04	0.01	Bok	V
1.099	18.98	0.06	SARA	V
1.099	19.03	0.01	Bok	V
1.102	18.99	0.02	Bok	V
1.103	19.00	0.01	Bok	V
1.105	19.00	0.01	Bok	V
1.106	18.98	0.01	Bok	V
1.108	19.04	0.05	SARA	V
1.108	18.98	0.01	Bok	V
1.109	18.98	0.02	Bok	V
1.110	18.97	0.01	Bok	V
1.113	18.90	0.03	Bok	V
1.115	18.90	0.03	Bok	V
1.117	19.05	0.06	SARA	V
1.118	18.85	0.04	Bok	V
1.120	18.90	0.03	Bok	V
1.123	18.92	0.03	Bok	V
1.125	18.88	0.03	Bok	V
1.128	18.87	0.03	Bok	V

Table 1—Continued

Time	Mag or Flux	Error	Instrument	Band
1.130	18.91	0.03	Bok	V
1.132	18.92	0.03	Bok	V
1.135	18.96	0.02	Bok	V
1.137	19.19	0.05	SARA	V
1.137	18.97	0.03	Bok	V
1.140	18.98	0.01	Bok	V
1.143	18.95	0.02	Bok	V
1.145	18.96	0.03	Bok	V
1.148	18.95	0.04	Bok	V
1.150	18.92	0.03	Bok	V
1.164	19.08	0.02	SARA	V
1.164	18.96	0.04	Bok	V
1.166	19.13	0.20	TNT 0.8m	V
1.166	18.92	0.02	Bok	V
1.169	18.97	0.04	Bok	V
1.172	18.98	0.02	Bok	V
1.175	19.01	0.02	Bok	V
1.175	19.40	0.20	TNT 0.8m	V
1.178	19.03	0.02	Bok	V
1.180	18.91	0.03	SARA	V
1.180	18.98	0.02	Bok	V
1.183	18.97	0.02	Bok	V
1.186	18.98	0.15	TNT 0.8m	V
1.186	19.01	0.03	Bok	V
1.193	18.94	0.04	SARA	V
1.194	19.07	0.15	TNT 0.8m	V
1.209	19.16	0.05	SARA	V
1.210	19.03	0.02	Bok	V
1.213	19.08	0.01	Bok	V
1.215	19.06	0.01	Bok	V
1.219	19.07	0.01	Bok	V
1.221	19.07	0.02	Bok	V
1.224	19.11	0.02	Bok	V
1.224	19.06	0.04	SARA	V
1.226	19.07	0.02	Bok	V
1.227	19.14	0.10	TNT 0.8m	V
1.229	19.09	0.02	Bok	V

Table 1—Continued

Time	Mag or Flux	Error	Instrument	Band
1.231	19.06	0.01	Bok	V
1.234	19.14	0.02	Bok	V
1.236	19.14	0.02	Bok	V
1.241	19.10	0.10	TNT 0.8m	V
1.241	19.10	0.07	EST 1m	V
1.258	19.35	0.12	TNT 0.8m	V
1.287	19.28	0.12	TNT 0.8m	V
1.288	19.37	0.10	EST 1m	V
1.299	19.23	0.12	TNT 0.8m	V
1.312	19.24	0.12	TNT 0.8m	V
1.355	18.98	0.11	UVOT	V
1.360	19.07	0.14	TNT 0.8m	V
1.376	19.12	0.12	TNT 0.8m	V
1.411	19.38	0.12	TNT 0.8m	V
1.422	19.44	0.12	UVOT	V
1.423	19.22	0.13	TNT 0.8m	V
1.472	19.57	0.13	TNT 0.8m	V
1.536	19.64	0.20	TNT 0.8m	V
1.572	19.76	0.10	HCT	V
1.582	19.44	0.06	HCT	V
1.721	20.00	0.07	UVOT	V
1.822	19.81	0.06	SARA	V
1.848	19.83	0.05	PROMPT	V
1.914	19.93	0.05	SARA	V
1.987	20.07	0.01	MDM	V
2.199	20.24	0.15	TNT 0.8m	V
2.237	20.40	0.14	TNT 0.8m	V
2.964	20.76	0.05	SARA	V
3.000	20.88	0.02	MDM	V
3.003	20.81	0.02	MDM	V
3.006	20.91	0.03	MDM	V
3.008	20.89	0.02	MDM	V
4.356	21.45	0.22	HCT	V
4.642	21.60	0.16	TNT 0.8m	V
0.900	18.76	0.02	PROMPT	R
0.998	18.78	0.02	Bok	R
0.999	18.80	0.02	Bok	R

Table 1—Continued

Time	Mag or Flux	Error	Instrument	Band
1.001	18.77	0.02	Bok	R
1.002	18.80	0.01	Bok	R
1.003	18.80	0.01	Bok	R
1.005	18.79	0.02	Bok	R
1.006	18.81	0.02	Bok	R
1.008	18.80	0.01	Bok	R
1.009	18.78	0.01	Bok	R
1.010	18.78	0.02	Bok	R
1.019	18.81	0.02	Bok	R
1.013	18.79	0.01	Bok	R
1.015	18.80	0.02	Bok	R
1.016	18.84	0.01	Bok	R
1.017	18.84	0.02	Bok	R
1.019	18.83	0.02	Bok	R
1.063	18.61	0.21	KAIT	R
1.065	18.60	0.16	KAIT	R
1.070	18.75	0.11	KAIT	R
1.070	18.59	0.11	KAIT	R
1.075	18.67	0.09	KAIT	R
1.078	18.66	0.07	KAIT	R
1.081	18.68	0.07	KAIT	R
1.084	18.63	0.07	KAIT	R
1.087	18.60	0.08	KAIT	R
1.087	18.66	0.08	KAIT	R
1.093	18.59	0.08	KAIT	R
1.095	18.63	0.08	KAIT	R
1.095	18.71	0.08	KAIT	R
1.102	18.40	0.13	KAIT	R
1.104	18.42	0.10	KAIT	R
1.104	18.51	0.14	KAIT	R
1.110	18.41	0.27	KAIT	R
1.120	18.44	0.11	KAIT	R
1.120	18.58	0.15	KAIT	R
1.125	18.26	0.12	KAIT	R
1.151	18.52	0.14	TNT 0.8m	R
1.159	18.88	0.17	TNT 0.8m	R
1.201	18.53	0.13	TNT 0.8m	R

Table 1—Continued

Time	Mag or Flux	Error	Instrument	Band
1.209	18.76	0.10	TNT 0.8m	R
1.222	18.71	0.10	EST 1m	R
1.266	19.00	0.10	EST 1m	R
1.273	18.85	0.09	TNT 0.8m	R
1.331	18.68	0.15	TNT 0.8m	R
1.339	18.79	0.15	TNT 0.8m	R
1.343	18.58	0.15	TNT 0.8m	R
1.346	18.74	0.16	TNT 0.8m	R
1.394	18.93	0.10	TNT 0.8m	R
1.450	18.96	0.10	TNT 0.8m	R
1.462	18.82	0.17	TNT 0.8m	R
1.513	19.00	0.14	TNT 0.8m	R
1.555	18.77	0.06	HCT	R
1.563	18.92	0.02	HCT	R
1.796	19.43	0.05	Kuiper	R
1.802	19.49	0.04	Kuiper	R
1.807	19.53	0.05	Kuiper	R
1.813	19.52	0.04	Kuiper	R
1.905	19.58	0.03	PROMPT	R
1.912	19.63	0.02	Kuiper	R
1.964	19.60	0.04	MDM	R
1.968	19.70	0.02	MDM	R
1.971	19.64	0.02	MDM	R
1.975	19.64	0.01	MDM	R
1.979	19.64	0.01	MDM	R
1.983	19.61	0.02	MDM	R
2.036	19.70	0.01	Kuiper	R
2.130	19.90	0.01	Kuiper	R
2.160	20.23	0.15	TNT 0.8m	R
2.213	19.93	0.18	EST 1m	R
2.275	20.00	0.11	TNT 0.8m	R
2.312	19.97	0.10	TNT 0.8m	R
2.350	20.15	0.10	TNT 0.8m	R
2.387	20.29	0.10	TNT 0.8m	R
2.427	20.10	0.10	TNT 0.8m	R
2.464	20.07	0.10	TNT 0.8m	R
2.500	20.17	0.12	TNT 0.8m	R

Table 1—Continued

Time	Mag or Flux	Error	Instrument	Band
2.533	20.01	0.12	TNT 0.8m	R
2.644	20.25	0.04	Loiano	R
2.659	20.23	0.05	Loiano	R
2.677	20.16	0.04	Loiano	R
2.781	20.44	0.06	Loiano	R
2.795	20.36	0.04	Loiano	R
2.843	20.46	0.04	Kuiper	R
2.854	20.42	0.03	Kuiper	R
2.865	20.40	0.02	Kuiper	R
2.989	20.40	0.02	MDM	R
2.992	20.38	0.02	MDM	R
2.995	20.40	0.02	MDM	R
2.997	20.41	0.02	MDM	R
3.006	20.47	0.03	Kuiper	R
3.631	20.73	0.14	Loiano	R
4.034	20.92	0.04	MDM	R
4.038	21.00	0.03	MDM	R
4.042	20.99	0.05	MDM	R
4.046	21.03	0.05	MDM	R
4.678	20.97	0.12	TNG	R
4.866	22.23	0.08	Kuiper	R
12.001	23.80	Upper limit	MDM	R
26.800	26.10	0.30	LBT	R
0.929	18.21	0.02	PROMPT	I
1.020	18.25	0.02	Bok	I
1.022	18.22	0.02	Bok	I
1.023	18.23	0.03	Bok	I
1.025	18.21	0.03	Bok	I
1.026	18.21	0.02	Bok	I
1.028	18.19	0.03	Bok	I
1.029	18.19	0.03	Bok	I
1.030	18.17	0.03	Bok	I
1.039	18.15	0.03	Bok	I
1.591	18.41	0.09	HCT	I
1.599	18.61	0.09	HCT	I
1.947	19.01	0.05	PROMPT	I
1.992	19.08	0.02	MDM	I

Table 1—Continued

Time	Mag or Flux	Error	Instrument	Band
2.977	19.88	0.02	MDM	I
2.980	19.82	0.02	MDM	I
2.982	19.82	0.03	MDM	I
4.693	20.84	0.06	TNG	I
1.854	18.17	0.24	SOAR	J
2.090	18.35	0.04	MMT	J
2.916	18.82	0.26	PAIRITEL	J
1.907	17.58	0.22	SOAR	H
2.916	18.33	0.25	PAIRITEL	H
1.877	16.96	0.28	SOAR	Ks
2.916	17.86	0.25	PAIRITEL	Ks
0.550	5.44e-12	4.95e-13	XRT	X
0.610	4.23e-12	6.47e-13	XRT	X
0.621	3.51e-12	5.30e-13	XRT	X
0.679	4.16e-12	6.36e-13	XRT	X
0.688	3.62e-12	5.70e-13	XRT	X
0.737	4.19e-12	7.12e-13	XRT	X
1.349	2.19e-12	3.41e-13	XRT	X
1.437	2.00e-12	3.23e-13	XRT	X
1.483	2.19e-12	3.61e-13	XRT	X
1.909	6.85e-13	9.24e-14	XRT	X
2.248	5.83e-13	9.04e-14	XRT	X
2.552	6.01e-13	1.09e-13	XRT	X
2.988	4.08e-13	7.35e-14	XRT	X
3.359	4.05e-13	8.70e-14	XRT	X
3.896	3.37e-13	6.75e-14	XRT	X
4.470	1.73e-13	4.86e-14	XRT	X
8.884	6.21e-14	1.55e-14	XRT	X
10.423	4.99e-14	1.55e-14	XRT	X
15.139	1.62e-14	6.75e-15	XRT	X
39.760	2e-15	Upper limit	Chandra	X

Note. — Observations carried out by this collaboration, late-time LBT detection (Dai et al. 2007), and late-time Chandra observation (Cenko et al. 2007b). X-ray fluxes have units of erg cm^{-2} s^{-1}. Radio fluxes are given in μJy.

Table 2. LIGHT-CURVE FITTING

Band	Model	α_1	α_2	Break Time	χ^2/d.o.f.
opt/uv/nir	all data	0.47 ± 0.10	2.05 ± 0.04	1.39 ± 0.04	10.25
opt/uv/nir	no flaring	1.24 ± 0.09	2.49 ± 0.13	3.37 ± 0.36	3.35
opt/uv/nir	after two days	1.56 ± 0.27	2.47 ± 0.13	3.73 ± 0.52	2.98
X-ray	all data	$1.16^{+0.23}_{-0.87}$	$1.85^{+0.19}_{-0.15}$	$1.34^{+0.24}_{-0.51}$	1.6
X-ray	no flaring	$1.49^{+0.14}_{-0.09}$	$1.94^{+0.39}_{-0.30}$	$3.93^{+9.72}_{-1.85}$	0.80
X-ray	after two days	$1.0^{+0.62}_{-1.81}$	$1.99^{+0.46}_{-0.32}$	$3.34^{+9.03}_{-1.27}$	0.50

Note. — Results of fitting a Beuermann function (Beuermann et al. 1999) (as revised by Rhoads & Fruchter 2001) broken power-law function to the data set; opt/uv/nir refers to the combined data set of optical, UV, and near-IR data. The columns labelled "no flaring" have removed the data between 1 and 2 days from the fit.

Table 3. UV/OPTICAL/NIR SPECTRAL ENERGY DISTRIBUTION

dust	χ^2/d.o.f.	β	A_V (mag)
none	2.615	0.854 ± 0.036	none
MW	3.137	0.855 ± 0.058	0.00 ± 0.032
LMC	2.643	0.736 ± 0.129	0.067 ± 0.070
SMC	0.896	0.519 ± 0.104	0.139 ± 0.041

Note. — Spectral energy distribution for UV, optical, and near-IR data only. We see that the SMC dust is strongly preferred.

Table 4. X-RAY/UV/OPTICAL/NIR SPECTRAL ENERGY DISTRIBUTION

Model	Γ_1	E_{bk} keV	Γ_2	$E(B-V)$ (mag)	N_H (10^{21} cm^{-2})	χ^2/d.o.f.
PL+MW	1.99±0.01	-	-	$0^{+8\times10^{-4}}_{-0}$	$2.5^{+1.6}_{-1.3}$	3.74
PL+LMC	1.99±0.01	-	-	$0^{+8\times10^{-4}}_{-0}$	$2.5^{+1.6}_{-1.3}$	3.74
PL+SMC	1.99±0.01	-	-	$0^{+9\times10^{-4}}_{-0}$	$2.5^{+1.6}_{-1.3}$	3.74
BKNPL+MW	1.6±0.1	0.0019±0.0002	2.03±0.03	<0.02	$1.4^{+1.6}_{-1.3}$	1.72
BKNPL+LMC	1.5±0.1	0.0023±0.0001	$2.06^{+0.03}_{-0.02}$	0.03±0.01	1.8±1.3	1.17
BKNPL+SMC	1.6±0.1	$0.0024^{+0.0002}_{-0.0004}$	$2.06^{+0.02}_{-0.03}$	$0.02^{+0.04}_{-0.01}$	$1.8^{+1.7}_{-1.3}$	1.31
BKNPL+MW	Γ_2-0.5	0.0019±0.0002	$2.04^{+0.03}_{-0.02}$	0.02±0.01	$1.3^{+1.6}_{-1.2}$	1.73
BKNPL+LMC	Γ_2-0.5	$0.0023^{+0.0001}_{-0.0002}$	2.06±0.02	$0.028^{+0.007}_{-0.008}$	$1.8^{+1.7}_{-1.3}$	1.13
BKNPL+SMC	Γ_2-0.5	$0.0024^{+0.0003}_{-0.0005}$	$2.07^{+0.05}_{-0.03}$	$0.030^{+0.007}_{-0.014}$	$1.8^{+1.7}_{-1.3}$	1.30

Note. — Results of fits to the near-IR/optical/UV/X-ray SED at 4.26 days since trigger, with power law and broken power law continuum models absorbed by MW-, LMC-, and SMC-like extinction and by X-ray absorption assuming solar metallicity. Galactic absorption and extinction were fixed at $N_{H,Gal} = 4.8 \times 10^{20}$ cm^{-2} and $E(B-V) = 0.052$ mag, respectively, and only intrinsic (at $z = 1.547$) quantities are reported in the table. PL = power law (where $\Gamma = 1 + \beta$); BKNPL = broken power law; MW = Milky Way extinction curve; LMC = Large Magellanic Cloud extinction curve; SMC = Small Magellanic Cloud extinction curve (as parametrized by Pei 1992).

Table 5. ABSORPTION LINES

λ_{obs} (Å)	W_λ^a (Å)	Trans.	λ_{rest} (Å)	z_{abs}
3316.6	< 2.766	OI 1302	1302.168	1.5470
3375.3	3.838 ± 0.706			
3549.9	< 1.810	SiIV 1393	1393.755	
3888.5	< 1.180	SiII 1526	1526.707	1.5470
3947.1	2.586 ± 0.318	CIV 1548	1548.195	1.5495
		CIV 1550	1550.770	1.5452
3989.2	1.501 ± 0.428			
4096.7	< 1.180	FeII 1608	1608.451	
4255.5	< 1.124	AlII 1670	1670.787	1.5470

[a]Observed equivalent width.

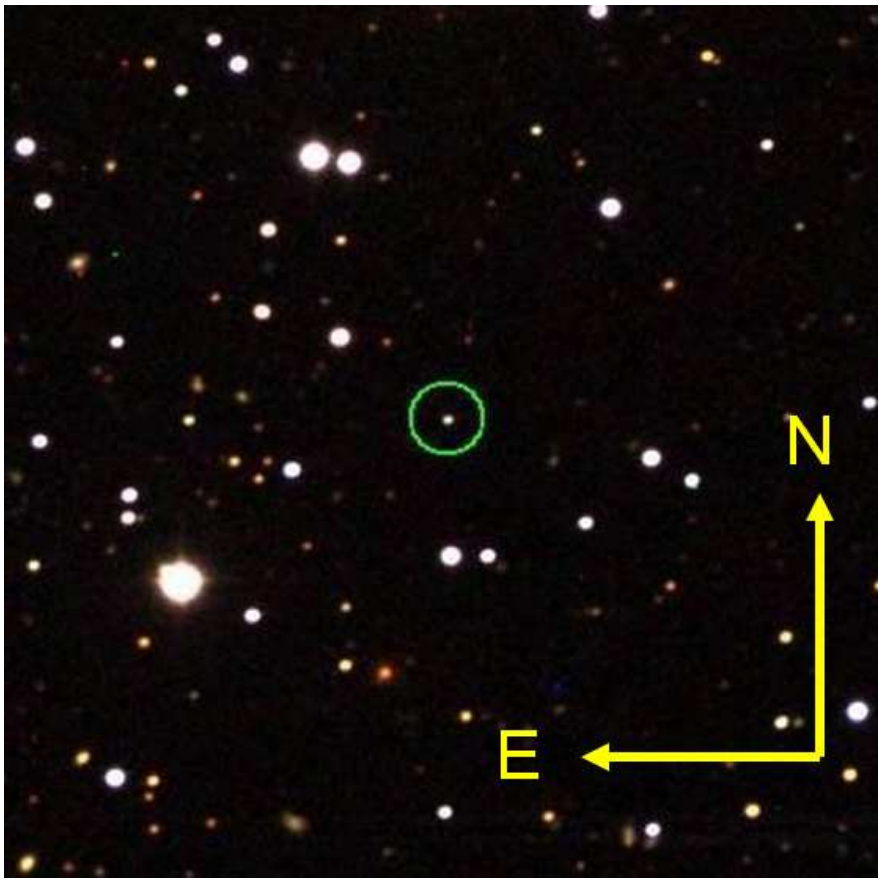

Fig. 1.— The field of GRB 070125 as imaged by the Bok telescope on Jan. 26, 2007, 08:11:08 (BVR). The field is 6.4' in diameter. The OT is circled. In this image, north is up and east is to the left.

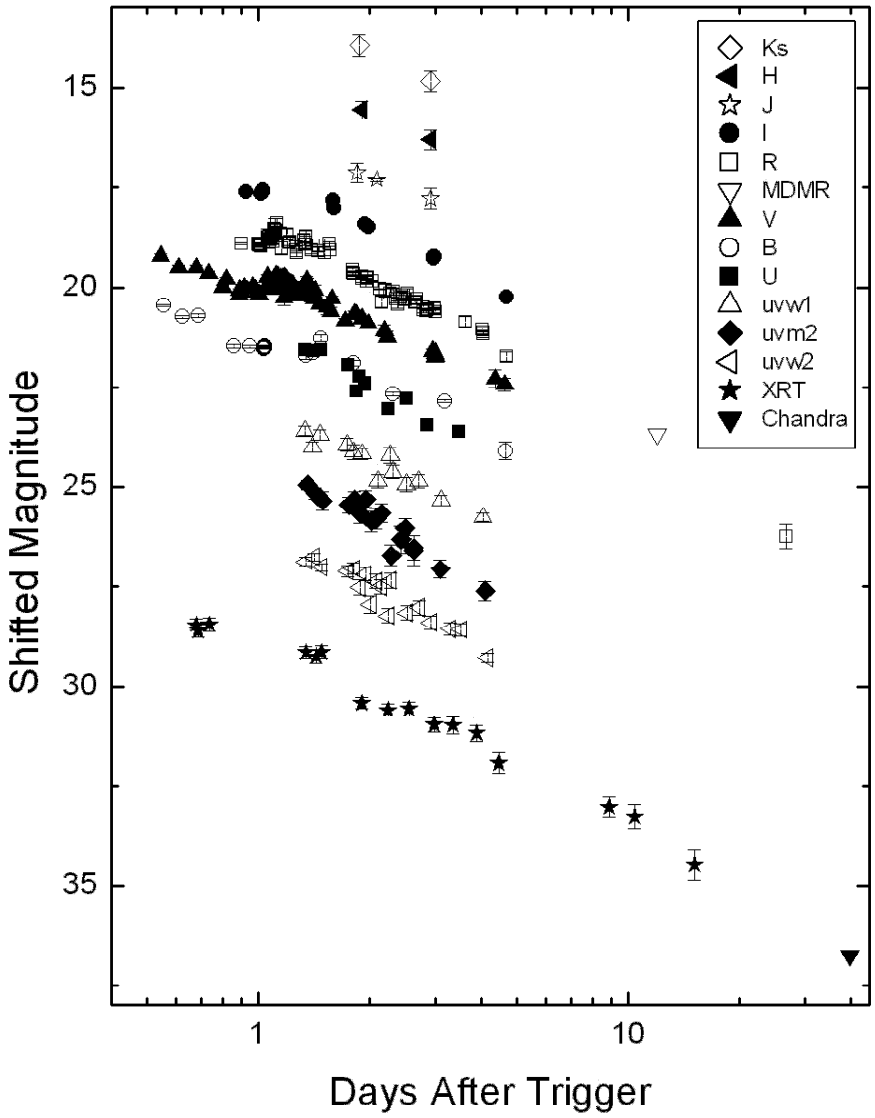

Fig. 2.— The combined data set (Vega magnitude system), corrected for Galactic extinction, arbitrarily scaled with respect to the R band for ease in reading. The XRT fluxes have been converted to magnitudes ($m = -2.5 \times \log F_\nu$). MDM and Chandra upper limits are represented by upside-down triangles. Band magnitude shifts are $Ks-$ 3.0, $H-$ 2.0, $J-$ 1.0, $I-$ 0.5, $V+$ 1.0, $B+$ 2.0, $U+$ 3.0, uvw1 + 5.0, uvm2 + 6.5, uvw2 + 8.0. All errors (excluding upper limits) are shown.

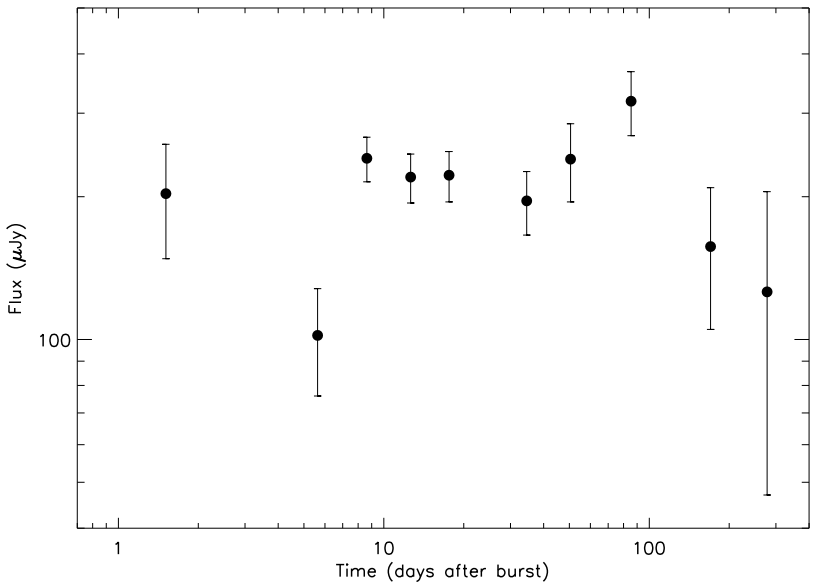

Fig. 3.— WSRT observations of GRB 070125 at 4.8 GHz.

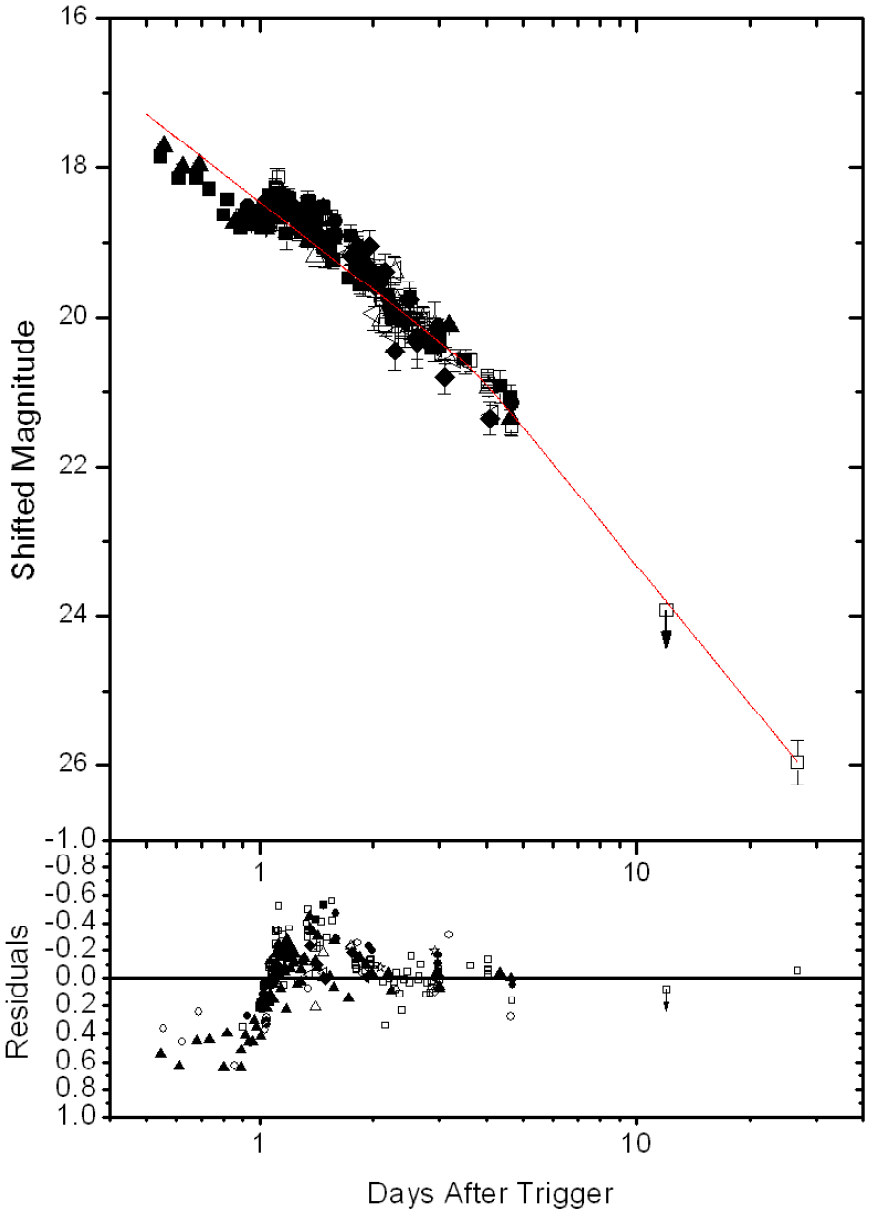

Fig. 4.— All UV, optical, and near-IR data contained in Figure 2 have been shifted to the R band based on the flux at 2 days post-trigger. Data before 2 days have been removed from this fit due to rapid flaring. The residuals to the fit are shown. We derive a jet break time of 3.73 ± 0.52 days.

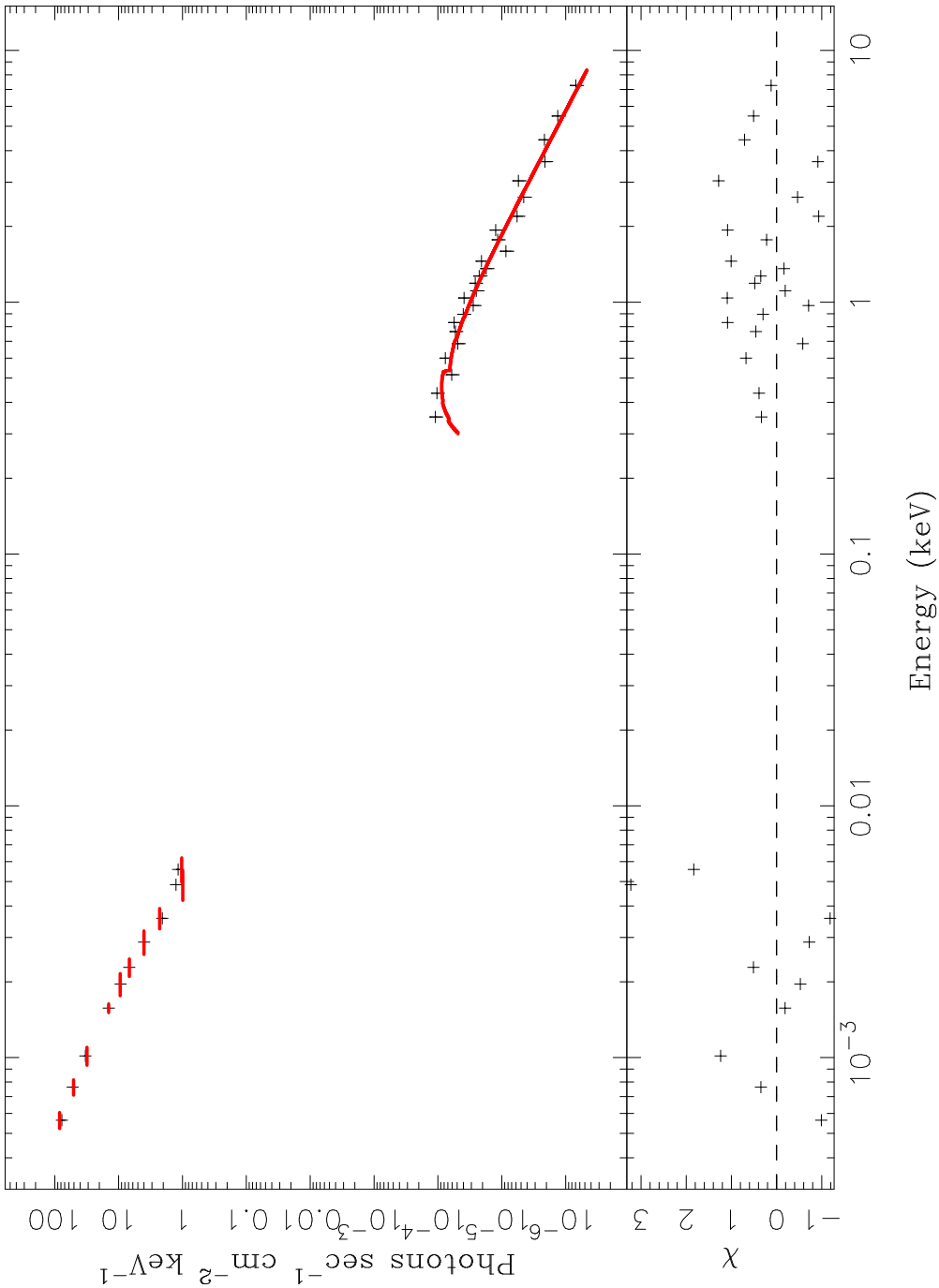

Fig. 5.— The unfolded SED at 4.26 days since trigger, including a *Swift* XRT spectrum and near-IR/optical/UV photometry (black points, upper panel). The line indicates the best-fitting model of an absorbed, broken power law plus LMC-like extinction. The lower panel shows the residuals of the fit.

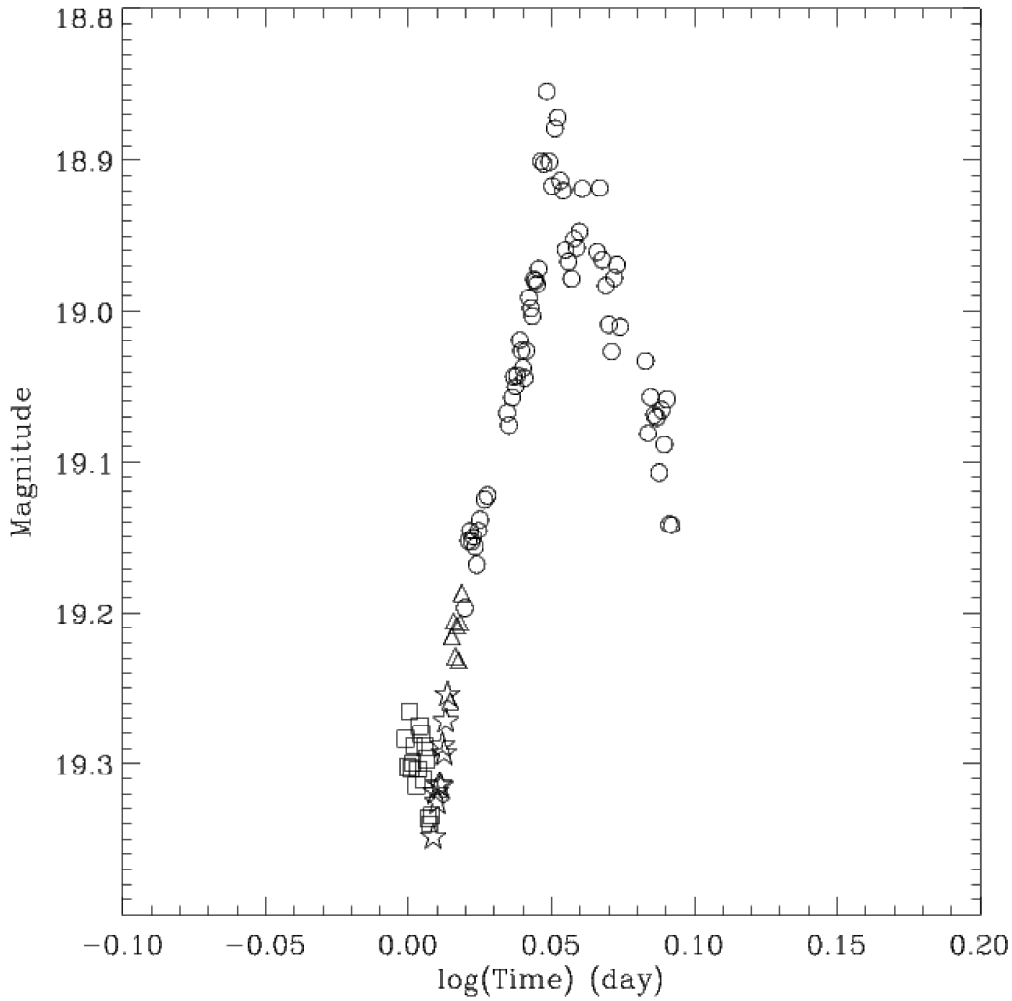

Fig. 6.— Bok $BVRI$ data shifted to the V band, showing high S/N detection of the second rebrightening episode, which has been confirmed by KAIT, TNT, and SARA data.

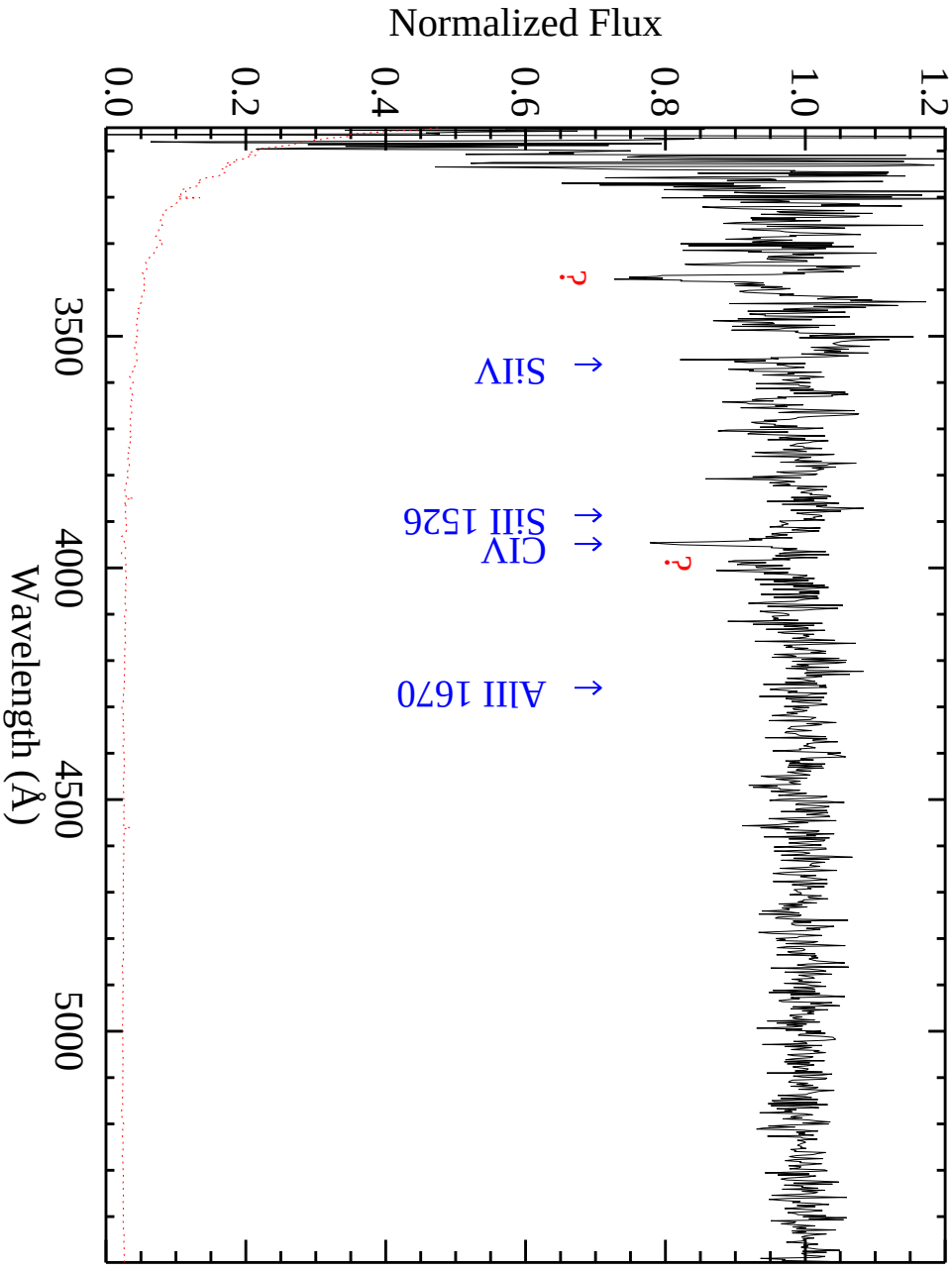

Fig. 7.— Normalized Keck/LRIS spectrum of the afterglow of GRB 070125. The figure shows the data acquired with the blue camera using the 400/3400 grism. The labeled arrows identify transitions associated with the metal absorption system at $z = 1.547$. This gas most likely arises in the host galaxy of GRB 070125. We also mark several significant absorption features which remain unidentified.

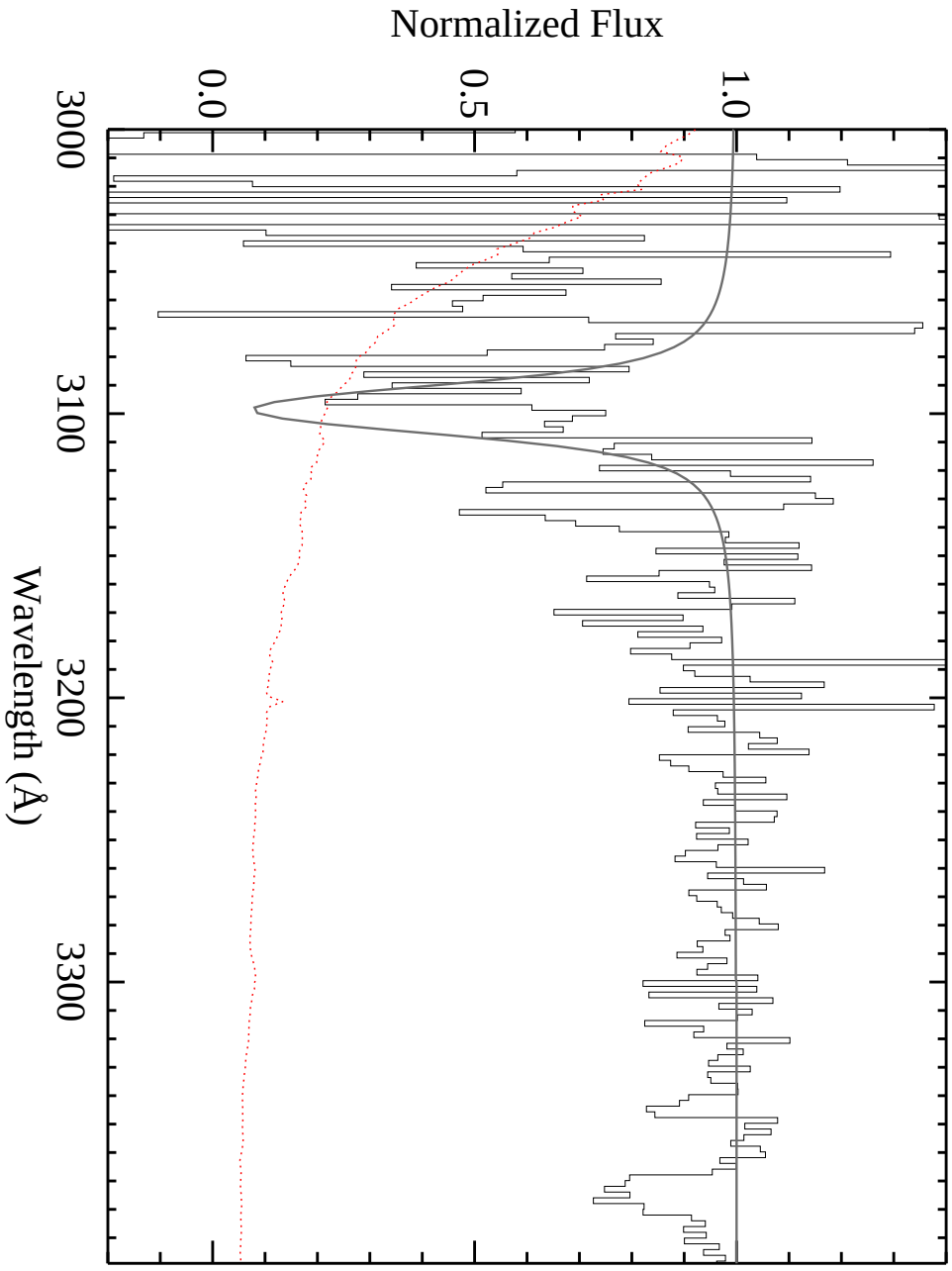

Fig. 8.— Close-up view of the spectral region near 3100 Å for the normalized Keck/LRIS spectrum of the GRB 070125 afterglow. The dotted line indicates the 1σ statistical error. The solid curve traces a damped Lyα profile with $N_{\rm HI} = 10^{20.3}\,{\rm cm}^{-2}$ centered at the redshift of the observed metal-line absorption system ($z = 1.547$; Figure 7). The data are formally inconsistent with a damped Lyα feature at this redshift, but we caution that systematic uncertainty (wavelength calibration and continuum placement error) do not rule out such a profile at very high confidence ($> 99\%$ c.l.). The data do rule out the presence of a strong Lyα absorber ($W_{Ly\alpha} > 5$ Å) redward of 3140 Å. Furthermore, there is no obvious signature of the Lyα forest in this spectrum. For these reasons, we argue that the metal-line absorber at $z = 1.547$ is gas associated with the host galaxy of GRB 070125. We cannot rule out, however, the possibility that the feature at $\lambda \approx 3375$ Å is relatively weak Lyα absorption at

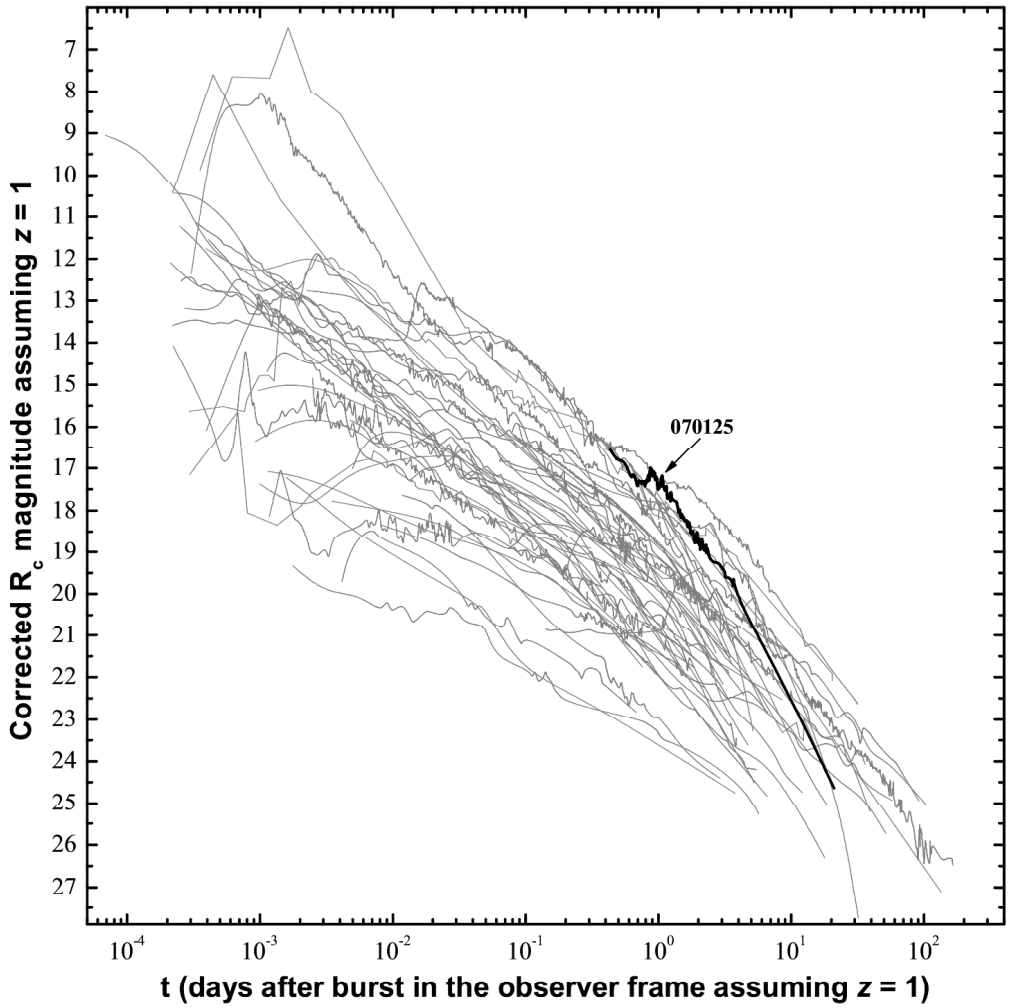

Fig. 9.— Afterglow light curves for 52 GRBs as they would look if all the bursts occurred at a redshift of 1 with no extinction (Kann et al. 2007). The thick line is the light curve of GRB 070125.